Observing Strain Dynamics in Au-Nanocubes with Ultrafast X-Ray Diffraction

Bachelor Thesis

B.Sc. Physics

Author: Franziska Jäger

First Reviewer: Prof. Dr. Matias Bargheer

Second Reviewer: Prof. Dr. Holger Lange

Supervisor: Dr. Steffen Peer Zeuschner

Institution: University of Potsdam, Institute for Physics and Astronomy

Field: Ultrafast Dynamics in Condensed Matter

Date: 18th August, 2026

1 Abstract

Metallic nanoparticles recently gained interest, due to their size- and shape-dependent optical properties and wide-range applications as nanosensors and plasmon-based photocatalysts. Within this context, one less explored field is chiral nanostructures and their light-matter interaction. In this thesis, the crystalline morphology and ultrafast strain dynamics in response to laser-excitation of cubic gold nanoparticles, exhibiting chiral nanostructuring and simpler cubic gold nanoparticles, are investigated, using static and ultrafast X-ray diffraction experiments. The results are compared to those obtained from a 100 nm gold thin film.

The static X-ray diffraction experiments reveal Au (002) and Au (111) Bragg peaks in the shape of Debye-Scherrer rings for both nanoparticle samples, while the thin film exhibits a twofold Au (111) Bragg peak. The time-resolved X-ray diffraction experiments reveal different ultrafast strain dynamics for the nanoparticles. Compared to the thin film, the simpler nanocubes exhibit a quasi-static strain amplitude that is 5 times larger, while the chiral nanocubes exhibit an amplitude that is 10 times larger under identical excitation conditions. Moreover, the chiral nanocubes display a more complex strain dynamic, modulated by smaller oscillations that could originate from chirality-driven phonon dynamics. Calculations of the temperature rise from the quasi-static strain amplitude yield a 4.2 K increase for the thin film, 70.4 K for the nanocubes, and 147.9 K for the chiral nanocubes.

A qualitative investigation of the different boundary conditions and absorption cross sections reveals a remaining effective absorbance of 7.4 % for the nanocubes and 8.5 % for the chiral nanocubes, indicating plasmon-enhanced absorption as a possible explanation. In contrast, typical gold thin films are known for their small absorbance of approximately 4 % and below. This difference in temperature change and absorbance compared to bulk materials underlines the importance of nanoparticles for efficient plasmon-based catalysis.

2 Kurzzusammenfassung

Aufgrund ihrer größen- und formabhängigen optischen Eigenschaften haben metallische Nanopartikel zuletzt zunehmend an Bedeutung gewonnen. Ein weniger erforschtes Gebiet in diesem Kontext sind chirale Nanostrukturen und ihre Licht-Materie-Wechselwirkung. In dieser Arbeit wird die kristalline Morphologie und die ultraschnelle Gitterdynamik von Gold-Nanowürfeln, mit und ohne chirale Strukturierung nach Laseranregung, untersucht. Dazu werden statische und ultraschnelle Röntgenbeugungsexperimente durchgeführt und mit den Ergebnissen eines 100 nm dicken Goldfilms verglichen.

Die statischen Röntgenbeugungsexperimente zeigen Au (002)- und Au (111)-Bragg-Peaks in Form von Debye-Scherrer-Ringen für die beiden Nanopartikelproben auf, während der Goldfilm einen zweiteiligen Au (111)-Peak aufweist. Durch zeitaufgelösten Röntgenbeugungsexperimente werden die unterschiedlichen Gitterdynamiken der Nanopartikel sichtbar. Im Vergleich zum dünnen Film zeigen die einfacheren Nanowürfel eine quasi-statische Gitterausdehnung, die fünfmal größer ist und die chiralen Nanowürfel eine, die 10,5-mal größer ist. Darüber hinaus liegt auf der transienten Gitterdynamik eine kleinere, höherfrequentigere Oszillation, die auf chiralitätsgetriebene Phononendynamiken hindeutet.

Berechnungen der Temperaturänderung aus der quasi-statischen Dehnungsamplitude ergeben einen Temperaturanstieg von 4,2 K für den dünnen Film, 70,4 K für die Nanowürfel und 147,9 K für die chiralen Nanowürfel. Eine qualitative Analyse der verschiedenen Randbedingungen und Absorptionsquerschnitte ergibt eine verbleibende effektive Absorption von 7,4 % für die Nanowürfel und 8,5 % für die chiralen Nanowürfel, was auf plasmonenverstärkte Absorption als mögliche Erklärung hindeutet. Im Vergleich dazu zeigen dünne Gold Filme eine typische Absorption von 4 %. Dieser Unterschied in der Temperaturerhöhung und Absorption unterstreicht die wichtige Rolle von Nanopartikeln in der plasmonengestützten Katalyse.

Contents

List of Figures

3 Introduction

Plasmonic gold nanoparticles recently gained interest due to their size- and shape-dependent optical properties, offering a wide range of applications in chemistry, physics, and medicine as nanosensors and plasmon-based photocatalysts [1]. Current research aims to better understand the factors governing the optical properties. One additional and less explored question is how chirality of nanostructures influences their light-matter interaction. Chirality, describing the broken inversion symmetry, is at the core of nature and a widespread phenomenon, with our very own hands and feet being the most familiar example [2]. Chirality has also been observed to manifest itself in physical properties, e.g., in the phononic system. In 2023, *K. Ishito et al.* experimentally observed chirality-driven phonons in a three-dimensional α-HgS crystal, using circularly polarized Raman scattering [3]. They suggest possible applications as nanosensors that exploit the chiral nature of the crystallic lattice and its potential interactions with the electronic and spin system. These findings motivate further research, in particular, on the crystal lattice of chiral nanostructures, such as the chiral gold nanoparticles investigated in this thesis. While their work focused on a bulk semiconductor, it raises the question whether chirality-driven phonons can impact ultrafast lattice dynamics.

This thesis addresses this question by investigating the dynamic strain response of chiral gold nanoparticles. To gain a deeper understanding of the crystallographic basis, in which the chiral phonons might manifest themselves, utilizing static and time-resolved X-ray diffraction experiments, motivates this thesis. The static characterization establishes the crystallographic foundation necessary for the time-resolved experiments by identifying the present Bragg reflections. The time-resolved studies, however, serve as the primary focus of this work and are discussed in greater detail.

Previous research on the specific type of chiral nanoparticles investigated in this thesis includes the study *Strain and crystallographic identification of the helically concaved gap surfaces of chiral nanoparticles* by *S. Choi et al.* [4]. They employed Bragg coherent X-ray diffraction imaging (BCDI) to index the crystallographic planes and surface Miller indices of the chiral nanoparticles, in order to map their complex morphology. They found the presence of a symmetric static strain field inside the nanoparticles. Simulations of the circular dichroism, based on the BCDI results, predicted plasmonic influences on the optical properties.

While their study provides a characterization of the static strain, this thesis aims to extend this by investigating the ultrafast strain dynamics in response to femtosecond laser-excitation. To gain a better understanding of possible chirality-driven strain dynamics, two types of gold nanoparticles, with and without chiral morphology, are investigated and compared to a thin film.

This thesis is divided into two main parts. The first focuses on the foundational static characterization, while the second one focuses on the time-resolved strain dynamics. The exact structure is as follows: Chapter 4 provides an overview of the nanoparticle samples investigated in this thesis, their synthesis and possible applications. Furthermore, the experimental technique, setup, and data evaluation routine, utilized for the static X-ray diffraction experiments, will be introduced and explained. In chapter 5, the experimental results, in the form of reciprocal space maps, are presented. Chapter 6 is used to qualitatively analyze the RSMs in order to identify the origins and interpret the observed features by calculations of the structure factor. Chapter 7 builds upon the findings of the previous chapters by focusing on the strain dynamics in response to femtosecond laser excitation. For that, the basics of pump-probe spectroscopy and strain dynamics in metals on a picosecond timescale are explained, in addition to the experimental techniques and setup. The experimental results are presented and described in detail in chapter 8. In chapter 9, the experimental findings for each of the samples are compared and qualitatively analyzed by calculating the temperature increase from the quasi-static strain levels and methodically deriving possible explanations for the observed temperature changes. Additional theoretical context is given and the results are discussed in the context of existing literature. Finally, chapter 10 summarizes the findings, discusses limitations of the chosen approaches and provides an outlook into possible future experiments.

4 X-Ray Diffraction on Gold Nanoparticles

4.1 Gold Nanoparticles

This chapter focuses on the properties of the samples studied in this thesis and give context to the discussion of the measurements following in the later chapters, as the observed time-resolved strain dynamics closely depend on the crystal structure and sample geometry. Thin films have been subject to extensive research over the years and their optical properties [5–7] and picosecond strain dynamics [8, 9] are well known. Their research includes studies on crystal growth [10], the laser-induced strain response in granular [11–13] and continuous thin films [8], heat transport in metallic heterostructures [14, 15], and superlattices [16, 17].

Nanoparticles need to be discussed separately from thin films, since their optical properties and strain dynamics differ, e.g., due to different in-plane boundary conditions and surface plasmon-enhanced absorption. These contributions, however, will be discussed in depth in section 9. Furthermore, the optical properties of nanoparticles depend on their shape, which has previously been documented for multiple variants such as spheres [18], rods [19], triangles [20], etc. and will now be investigated for nanocubes. Still, the properties and dynamics of nanoparticles, or more specifically, gold nanoparticles are not as well understood. Hence, this thesis focuses on recording the laser-induced strain dynamics of two different types of gold nanoparticles, with and without chiral structuring. Nonetheless, the recorded applications of gold nanoparticles (AuNPs) are widespread and chiral nanoparticles follow the same trend, with applications in chiral technologies having been reported, notably by *S.D. Namgung et al.* in 2022, introducing efficient circularly polarized light-sensitive hot-electron transistors [21]. Furthermore, AuNPs show possible applications as biosensors [22] and in nanomedicine for purposes of diagnostics [23], photothermal therapy [24] and in nanotechnology [25, 26].

The nanostructured samples investigated in this thesis were provided by Prof. Ki Tae Nam of Seoul National University's department of Material Science and Engineering and include gold nanocubes and l-chiral gold nanocubes. The prefix "l-" in l-chiral refers to the left-handed helicoidal geometry of the nanoparticle sample, as seen in fig. 2, which will be one of the factors influencing the observed dynamics in the time-resolved measurements. In addition, a gold thin film, provided by Dr. Matthias Kronseder of the University of Regensburg, will be investigated and discussed in the same context, serving as a reference for comparison.

4.1.1 The Gold Lattice

Gold crystallizes in a face-centered cubic (fcc) lattice with a lattice constant of 4.07 Å and is known for its chemical stability and high reflectivity, which is why it is often used as a mirror coating for optical components. Especially, when light in the infrared range is utilized [27, 28]. The schematic in fig. 1 depicts the conventional unit cell of gold.

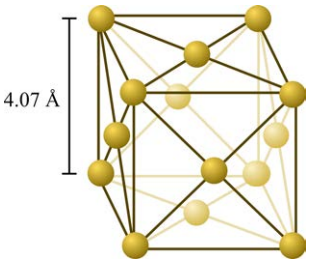

Figure 1: Fcc lattice structure of gold

The investigated gold thin film and gold nanoparticles are deposited on a magnesium oxide (MgO) substrate. Here, it is important to note that the way the gold samples grow and their crystallinity depend on the layer they are grown on. *Mattern et al.* [10] demonstrate the differences of growing gold films directly on MgO versus on iron layers of different thicknesses. When growing a gold film on bare MgO, it shows an exclusive Au (111) orientation with limited crystallinity and a high surface roughness of $\Delta_{\text{rms}} = \pm 12$ nm, whereas growing gold on a sufficiently thick (≈ 20 nm) layer of iron results in a smoother surface ($\Delta_{\text{rms}} = \pm 2$ nm) and more crystalline growth in Au (002) orientation.

4.1.2 Chiral Nanoparticles

In organic chemistry and in this work, "chirality" refers to objects or particles, which exhibit a non-symmetric geometry. A particle is regarded as "chiral", if it cannot be mapped onto its mirror image by translation or rotation and, inversely, "achiral" or "non-chiral", if it can be superimposed on its mirror image [29]. Furthermore, the prefix "l-" in "l-chiral" refers to the orientation of the spiral-like structure, with d-chiral being its mirror image, as can be seen in fig. 1 in ref. [30] where SEM images of l- and d-chiral nanoparticles are presented.

The synthesis of the helicoidal (l-chiral) and simpler, cubic nanoparticles is described in ref. [31] and includes the nucleation of spherical gold seeds, which are then grown into octahedral seeds in a cetyltrimethylammonium-bromide aqueous solution. The chiral overgrowth of helicoids is driven by l-glutathione. Finally, the particles are deposited in thin layers on the MgO substrate, using Langmuir-Blodgett techniques [32, 33].

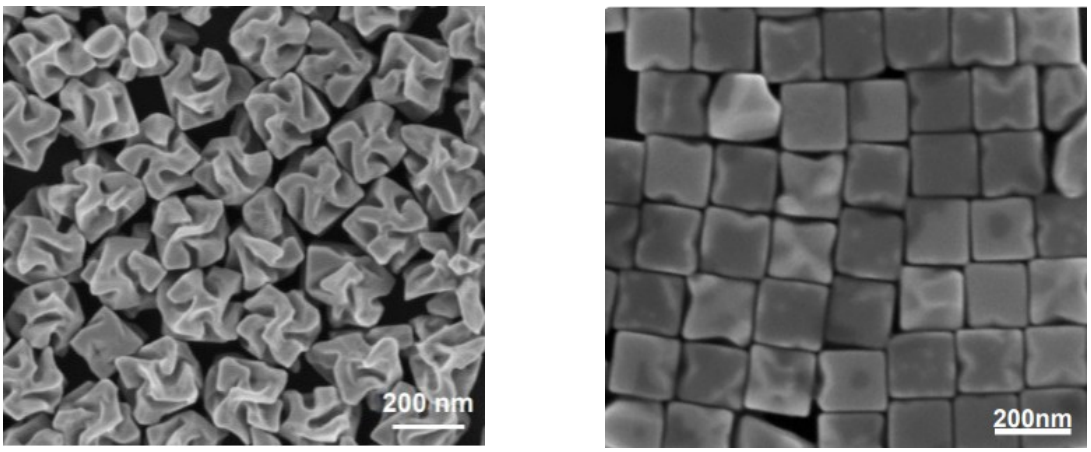

Figure 2: SEM images of l-chiral gold nanocubes (left) and gold nanocubes (right) on MgO substrate. The samples and SEM images were provided by Prof. Ki Tae Nam and coworkers.

Scanning electron microscopy (SEM) images of the gold nanocubes (AuNCs) and l-chiral gold nanocubes (LAuNCs) can be seen in fig. 2. According to the manufacturer, the samples consist of one to three layers of NCs and have a side length of about 180 nm. As the name suggests, the NCs exhibit a cubic geometry and are oriented quite uniformly and closely packed on the MgO substrate layer compared to the LAuNCs, which are not as neatly packed onto the substrate. While their overall geometry remains cubic, four symmetric cavities are present on each side of the cubes. The SEM reveals some diversity in the appearance of the chiral sample with some cubes appearing more cube-like than others. Moreover, some of the cubes appear to be tilted and rotated relative to the substrate layer.

The X-ray diffraction (XRD) experiments conducted in the following chapter will give more insight into the crystal structure of the samples and lay the foundation for the time-resolved measurements. The XRD method is particularly useful for layer-specific and nondestructive analysis of solids and allows analysis of the mosaicity and the size and shape of the coherently scattering domain [34]. An example of the capabilities of XRD and time-resolved X-ray diffraction is given by *S. P. Zeuschner et al.* in ref. [15] where the nanomorphology of a hafnium nitride (HfN) film was analyzed with the above mentioned-techniques. Before presenting the results of the static measurements, the technique itself, and its specifics have to be discussed.

4.2 Principles of X-Ray Diffraction

X-ray diffraction is an established technique to examine the crystal lattice of solid structures, including the AuNPs studied in this thesis [35]. Since XRD uses X-ray radiation with wavelengths on the order of an Angstrom ($1\,\text{Å} = 10^{-10}\,\text{m}$), the same order of magnitude as atomic structures, it can be used to measure the distance between atoms. In particular, XRD allows one to determine the average lattice plane spacing perpendicular to the sample surface, the out-of-plane direction.

In a typical XRD experiment, X-rays are generated by a source and focused onto the sample. The photons are elastically scattered by the electron shells and form spherical waves originating from each scattering center. These waves interfere to form the emitted signal. The diffracted intensity is then measured by a position-sensitive detector as a function of the scattering vector $\vec{Q}$. The scattering vector $\vec{Q} = (q_x, q_y, q_z)$, characterizing the diffraction process, is defined by the change in momentum of the incident and diffracted photons [35]:

$$\vec{Q} = \Delta\vec{k} = \vec{k}_{\text{out}} - \vec{k}_{\text{in}}. \tag{1}$$

Diffraction maxima can only be observed if this scattering vector coincides with a reciprocal lattice vector $\vec{G}$ in reciprocal space of the sample. This requirement defines the Laue condition for X-ray diffraction [35]:

$$\vec{Q} = \vec{G}. \tag{2}$$

A variation of the wave vectors $\vec{k}_{\text{in}}$ and $\vec{k}_{\text{out}}$ allows for scanning of the reciprocal space. The observed local maxima of the diffracted intensity in this reciprocal space are directly related to the sample's crystal lattice in real space, while their characteristics, namely the position, width, and intensity, yield information on the nanomorphology of the sample. While the position is directly linked to the average lattice constant, the intensity is correlated with the structure factor, or equivalently, to the lattice sum. The width yields information on the crystallinity and thickness of the sample. The average out-of-plane lattice plane spacing d_3 is linked to the lattice constant a and can be calculated via the reciprocal lattice vector $\vec{G}$:

$$|\vec{G}| = \frac{2\pi n}{d_3} \tag{3}$$

where d_3 can be written in terms of the Miller indices[1] [35]:

$$d_{hkl} = \frac{a}{\sqrt{h^2 + k^2 + l^2}} \tag{4}$$

where h, k, and l denote the Miller indices and n an integer multiple. For nanostructured samples, such as the AuNCs and LAuNCs, or crystals where the lattice planes are not parallel to the sample surface, diffraction is still governed by the Laue condition. However, the wave vector $\vec{k}_{\text{out}}$ can change from particle to particle, enabling asymmetric scattering. Thus, the corresponding reciprocal lattice vector $\vec{G}$ is no longer necessarily perpendicular to the sample surface. In reciprocal space, the sample surface is defined by the q_x-q_y plane, and $\vec{G}$ can exhibit a tilt relative to this plane. The reciprocal space vector q_z denotes the out-of-plane direction. This case illustrates why applying the Laue condition is useful. Since the lattice planes can be tilted relative to the sample surface (see fig. 3), one can no longer define a single angle, under which the X-ray photons are incident. Instead, one has to differentiate between

[1] Miller indices form the index system for lattice planes in Bravais lattices. For a cubic crystal like gold, a family of lattice planes is characterized by the three integers h, k, and l, which are orthogonal to the reciprocal lattice vector $\vec{G}$. More about the notation system can be read in [36] and [37].

the angle ω, which is defined relative to the lattice planes, and the angle α_{in}, which is defined relative to the sample surface. The emergent angles have to be defined similarly: θ is defined relative to the lattice planes and α_{out} relative to the sample surface. Asymmetric diffraction occurs, when α_{in} is not equal to α_{out}. Since the Laue condition is defined irrespective of angular configurations, it can be used to describe all diffraction scenarios, including symmetric and asymmetric diffraction as well as diffraction from laterally homogeneous and nanostructured samples.

A simplified formulation (for symmetric diffraction) of the Laue condition is Bragg's law [35]:

$$n\lambda = 2d_3 \sin\theta_{\text{Bragg}}. \tag{5}$$

It states that in this case, diffraction maxima from constructive interference can be observed if the optical path length difference between light scattered from neighboring lattice planes is at an integer multiple n of the X-ray wavelength λ. It relates the out-of-plane lattice spacing d_3 to the so-called Bragg angle θ_{Bragg}. If the light is incident on the sample under this angle θ_{Bragg}, a characteristic maximum, a Bragg peak, can be observed.

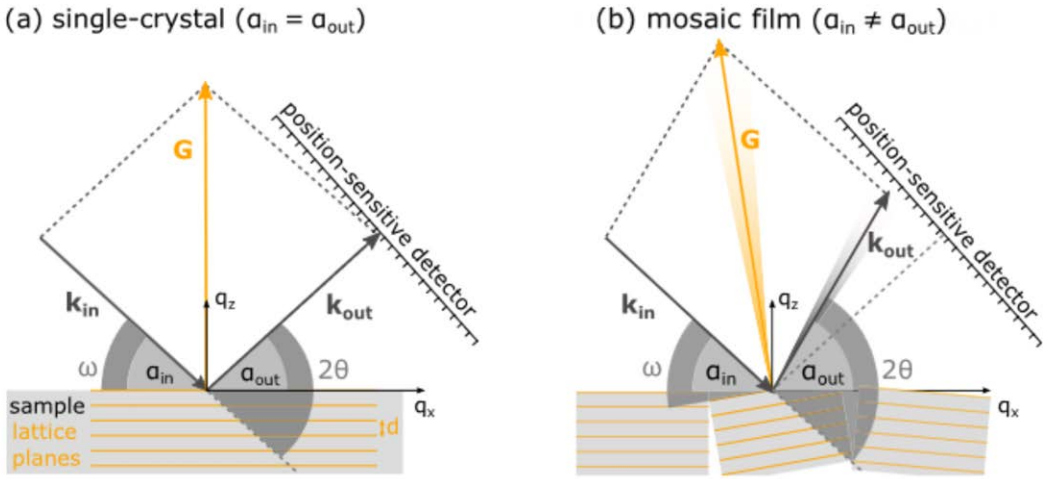

Figure 3: a) Symmetric diffraction ($\alpha_{\text{in}} = \alpha_{\text{out}}$) geometry for the case of the lattice planes being parallel to the sample surface. The incident angles $\alpha_{\text{in}} = \omega$ and emergent angles $\alpha_{\text{out}} = \theta$ coincide. **b)** Scattering on nanostructured samples for which the crystallites are tilted relative to the sample surface ($\alpha_{\text{in}} \neq \alpha_{\text{out}}$). This results in the scattering vector $\vec{G}$ being tilted relative to the sample surface. The figure is taken from [11].

A schematic depiction of the different diffraction cases is shown in fig. 3. The broadened diffraction maxima along q_x in the case of asymmetric scattering can either be caused by the nanostructuring of the sample, i.e., by scattering on nanoparticles or by the tilt of the nanoscale crystallites relative to the sample surface within the sample itself, in other words, by mosaicity. For three-dimensional samples, it follows that the diffraction maxima can be broadened along q_x and q_y, since the crystallites or nanoparticles cannot just be tilted but also rotated with respect to the sample surface. For symmetric scattering, the incident and emergent angles coincide: $\alpha_{\text{in}} = \omega$ and $\alpha_{\text{out}} = \theta$ [11].

4.3 Interpreting XRD signals

Next to the position, the intensity and width of the observed diffraction maxima help to identify characteristics of the measured sample.

The width of a peak, measured along the q_z-axis, is given by the number of reflecting planes in the sample. For larger numbers of reflecting planes, the peak will be narrower, for smaller numbers the peak will be broadened. If a peak is broadened along the q_x- or q_y-axis, one can conclude that the sample is polycrystalline. The nanostructured gold samples exhibit such broadening in the q_x- and q_y-dimensions (seen in fig. 8 and fig. 9) because of their powder-like nature.

The observed intensity or scattering amplitude of the peaks depends on multiple factors. On the one hand, it depends on the structure factor, which can be imagined as a factor that describes the scattering efficiency of a unit cell into different $\vec{Q}$ directions. On the other hand, it depends on the lattice sum, which depends on the number of lattice planes [35]:

$$\sqrt{I(\vec{Q})} \propto \mathcal{F}(\vec{Q}) = \overbrace{\sum_{j=1}^{N} f_j(\vec{Q}) e^{i\vec{Q}\cdot\vec{r}_j}}^{\text{structure factor } S_{hkl}} \overbrace{\sum_{n=1}^{M} e^{i\vec{Q}\cdot\vec{R}_n}}^{\text{lattice sum } \mathcal{G}} . \tag{6}$$

The intensity $I(\vec{Q})$, measured as a function of the scattering vector $\vec{Q}$, is directly proportional to the square of the scattering amplitude $\mathcal{F}(\vec{Q})$, which is defined by the product of two sums that correspond to the structure factor and the lattice sum, respectively (see eq. (6)). The structure factor S_{hkl} depends on the atomic scattering factor $f_j(\vec{Q})$ and the position $\vec{r}_j$ of the j-th atom in the unit cell. N is the number of atoms per unit cell. The lattice sum is defined via the position $\vec{R}_n$ of the n-th unit cell and M is the number of scattering unit cells. The Miller indices h, k and l denote the lattice planes considered in the scattering process. The brightest diffraction peaks are observed for large, near-perfect single crystals where the periodic lattice ensures coherent constructive interference from all unit cells for the same reciprocal lattice point. The diffracted intensity is concentrated into a narrow and bright reflection instead of a broadened one.

Some reflections or diffraction peaks cannot be observed and are considered forbidden. For these, the structure factor and intensity are equal to zero. An example of this is given in the discussion of the measurement results in section 6.

The nanostructured nature of a sample leads to a broadening of the observed diffraction peaks in the reciprocal space along the q_x- and q_y-directions into so-called Debye-Scherrer rings. Moreover, broadening along the q_z-direction can almost always be observed, since it is governed by the thickness of the sample. In practice, and in the following XRD measurements, the narrowest peaks are produced by the substrate (MgO) layer, since it is many times thicker than the gold layer grown on top.

Now knowing the contributing factors of the lattice to the observed intensity, namely the size of the crystal, the structure factor, lattice sum and possible distortions of the atomic lattice, one has to consider the limits of the utilized measurement instruments. Since the experimental setup (seen in fig. 4) uses a convergent X-ray source and the generated X-rays are not truly monochromatic, the observed peaks are additionally broadened. This means that the actual measured intensity is a convolution of the instrument's resolution area $I(RA)$ and the reciprocal space $I(RS)$ of the sample [38]:

$$I(\vec{Q}) = (RS * RA)(\vec{Q}). \tag{7}$$

While the shape of the resolution area is given by the energy distribution and trajectories of the X-rays, the shape of the reciprocal space is given by the coherence length of the sample's crystal structure [38]. The shape of the reciprocal space near the diffraction condition can be approximated by a Gaussian function whose width corresponds to the inverse coherence length.

Having established the theoretical basics of XRD and how to interpret data from static measurements, the experimental setup is discussed in the following section.

4.4 Experimental Setup for Static Measurements

To map the crystal structure of the samples, reciprocal space maps are recorded, which are inversely related to the spacing of the crystal lattice in real space.

This is translated into practice by performing static XRD experiments. This chapter describes the experimental process and subsequent data processing routine to obtain such reciprocal space maps. The static XRD setup is part of a larger setup that includes the possibilities of both static- and time-resolved diffraction experiments. The latter will be utilized and described in section 7.2 and for now, only the static measurements will be discussed. A detailed description of the static setup is given in the master's thesis of *A. von Reppert* [39]. In short, the main components of the static setup include the X-ray source, the focusing optics, the sample holder, the sample, and a position-sensitive area X-ray detector (PSD), which are schematically depicted in fig. 4.

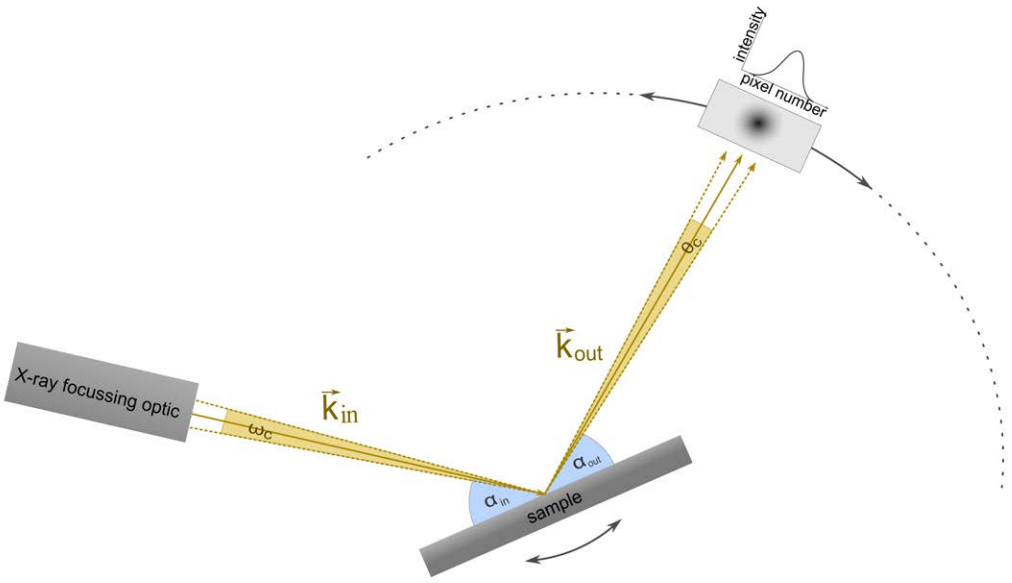

Figure 4: The CuK$_\alpha$-part of the generated X-ray spectrum is focused onto the sample in the two-circle goniometer under the angle α_{in}. The source itself introduces a convergence angle of $\omega_c \approx 0.3°$. A position-sensitive area X-ray detector captures the diffracted photons at the angle α_{out} relative to the sample surface. In the goniometer, the sample and detector can be rotated relative to one another to carry out the $\theta - 2\theta$-scans by symmetrically increasing α_{in} and α_{out}. The figure is adapted from [39].

For the static measurements, a continuous wave X-ray tube, utilizing a copper anode as the source, can be used. In the tube, the X-rays are created by accelerating and focusing the electrons emitted from a hot cathode onto a copper anode by applying an external voltage. The accelerated electrons interact with the atoms of the anode material, causing elastic electron-electron collisions and creating holes in the K-shell, which are then refilled by higher-energy electrons under energy release. These energies match the energetic differences between the atomic levels of copper and mark the origin of the characteristic emission lines in the X-ray spectrum. Conversely, the continuous background of bremsstrahlung in the spectrum stems from the deceleration of electrons from inelastic electron-electron collisions where the electrons do not create holes in the atomic shells of copper and can therefore possess energies outside of the characteristic energies. In the here presented experiments, a plasma-based X-ray source (PXS) was used instead of a continuous wave tube, which also generates CuK$_\alpha$ radiation. Details of the PXS setup are given in section 7.2.

Following generation, the Montel multilayer X-ray optic focuses the CuK$_\alpha$-part of the spectrum onto the sample with a convergence angle of $\omega_c \approx 0.3°$. The diffracted intensity distribution is then measured by the PSD, which returns a binary signal if at least one photon has been detected during the exposure time.

For each of the mentioned gold samples, a symmetric $\theta - 2\theta$ scan is carried out. This means that each sample is mounted onto the sample holder in the inner circle of the two-circle goniometer and moved so that the incident angle α_{in} of the photons is symmetric to the angle θ, under which the photons are diffracted. This angle, in turn, is given by the Bragg (eq. (5)) or Laue (eq. (2)) condition. The PSD on the outer circle captures multiple angles α_{out} and probes the intensity of the diffracted photons perpendicular and parallel to the diffraction plane. For scanning the reciprocal space, the program PilatusTheta2Theta is used. It steers the two-circle goniometer to measure different α_{in}-α_{out} combinations in an angular interval, which has to be chosen beforehand based on literature values of the expected Bragg reflections.

Reciprocal Space Maps

Scanning the reciprocal space corresponds to a Fourier transform of the electrons' density distribution and by extent of the atoms' positions or the direct crystal lattice [35, 40]. Completing scans of the diffracted X-rays at different angular combinations and processing the measured intensities as a function of the scattering vector $I(\vec{Q})$ yields a reciprocal space map, from which material-specific parameters such as the lattice constant and the order of crystallinity can be derived. Details on how reciprocal space maps are obtained are given in the master's theses of *J.-E. Pudell* [41] and *A. von Reppert* [39]. In a $\theta - 2\theta$ scan with a point-detector, only photons from symmetric angle combinations are taken into consideration, corresponding to scanning along the q_z-axis in reciprocal space. However, using an area detector allows for three-dimensional imaging of the reciprocal space. As the area detector is moved along the outer goniometer circle for recording different $\alpha_{in} - \alpha_{out}$ combinations, each detector pixel is assigned a new scattering vector $\vec{Q}$.

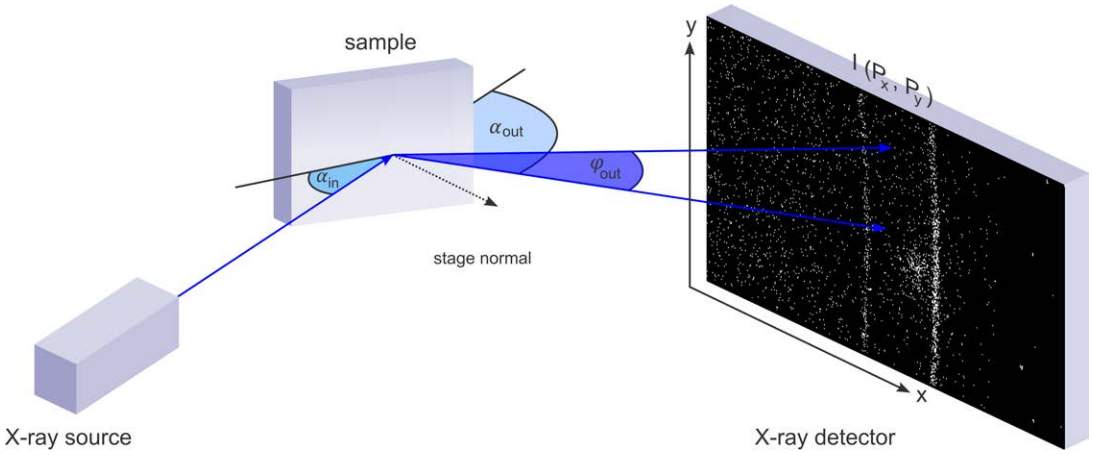

Figure 5: Schematic depiction of the defined angles in the diffraction setup.

During measurements, the detector counts how many photons are incident at each pixel during the exposure time. This way, a two-dimensional intensity distribution $I(P_x, P_y)$ is created for every angle α_{in} and α_{out} whereby α_{out} is associated with the center pixel. Concatenating the individual scans ultimately results in an intensity map $I(\alpha_{in}, \alpha_{out}, \varphi_{out})$ in the direct angular space. Every pixel is assigned a specific angular combination by considering the pixel's size and detector distance. Fig. 5 depicts a schematic illustration of the diffraction conditions. The intensity map reveals maxima that are related to the average lattice constant given by Bragg's law (eq. (5)) and whose positions are directly linked to the lattice

constant. However, to obtain an undistorted image of the Bragg peaks, a transformation from the angular (α_{in}, α_{out}, φ_{out})-space to the reciprocal (q_x, q_y, q_z)-space has to be performed. Details of the transformation are given in [42]. In short, the transformation utilizes:

$$\vec{q} = \begin{pmatrix} q_x \\ q_y \\ q_z \end{pmatrix} = k \begin{pmatrix} \cos\alpha_{out} \sin\varphi_{out} - \cos\alpha_{in} \sin\varphi_{in} \\ -\cos\alpha_{out} \cos\varphi_{out} + \cos\alpha_{in} \cos\varphi_{in} \\ \sin\alpha_{out} + \sin\alpha_{in} \end{pmatrix} \tag{8}$$

where $k = 2\pi/\lambda$ describes the absolute value of the scattered wave vector and $\varphi_{in}, \varphi_{out}$ the azimuthal (in-plane) angles of the incident and diffracted photons, respectively. These calculations are done with nx5d, a data analysis framework that converts the intensity maps into RSMs. It is generally used for automated XRD data evaluation and details can be found in [43].

Because of this nonlinear transformation, the area of each grid cell in the reciprocal space has to be corrected to be square-shaped again. After also transforming the intensities, reciprocal space maps with characteristic Bragg peaks are produced, from which the material-specific lattice constant can be derived from the peak positions.

5 Results of the Static XRD Measurements

For each of the gold samples, such a RSM was recorded by first mounting the samples onto the sample holder in the goniometer and then capturing the diffracted photons with the area detector. Scanning the reciprocal space produces the RSMs seen in fig. 6, fig. 8, and fig. 9.

5.1 Gold Thin Film

A subset of the three-dimensional reciprocal space of the 100 nm gold thin film is visualized in fig. 6 as different two-dimensional projections. The q_z-q_x and q_z-q_y maps reveal two maxima at different q_z-coordinates. The center q_z-positions of the Au (111) and MgO peaks are estimated by eye to 2.62 Å^{-1} and 2.94 Å^{-1}, respectively.

The Au (111) peak appears as bright as the substrate MgO peak, indicating a high crystallinity. The Au (111) reflection exhibits a broad and narrow portion along q_x, indicating two zones of differing morphology in the in-plane dimension of the gold film. Since the peak intensity is proportional to the lattice sum, it is reasonable to assume that the broader portion encompasses a more disordered morphology and, hence, a smaller coherence length. Conversely, the smaller portion encompasses a more ordered morphology and higher crystallinity, resulting in a larger coherence length. This leads to the assumption that the gold film portion closer to the substrate grew more orderly, while the portion closer to the surface grew in a more disordered fashion and includes more lattice defects. Similar observations of differing crystalline growth and coherence lengths have been recorded for HfN thin films by *S. P. Zeuschner et al.* [15].

One parameter of interest, obtained from the RSMs, are the peak positions and, hence, the average lattice constants a of the samples. For a cubic-crystal lattice, the interplanar lattice spacing d and the out-of-plane component of the scattering vector q_z are defined via eq. (4). Inserting

$$q_z = \frac{2\pi}{d_{hkl}} \tag{9}$$

into eq. (4) yields an expression for the average lattice constant:

$$a = \frac{2\pi}{q_z}\sqrt{h^2 + k^2 + l^2}. \tag{10}$$

For the gold-sample peaks in fig. 6, this yields the following result:

$$a_{111} = \frac{2\pi}{2.62\ \text{Å}^{-1}}\sqrt{3} = 4.154\ \text{Å}, \tag{11}$$

which is close to the bulk gold literature value of 4.07 Å.

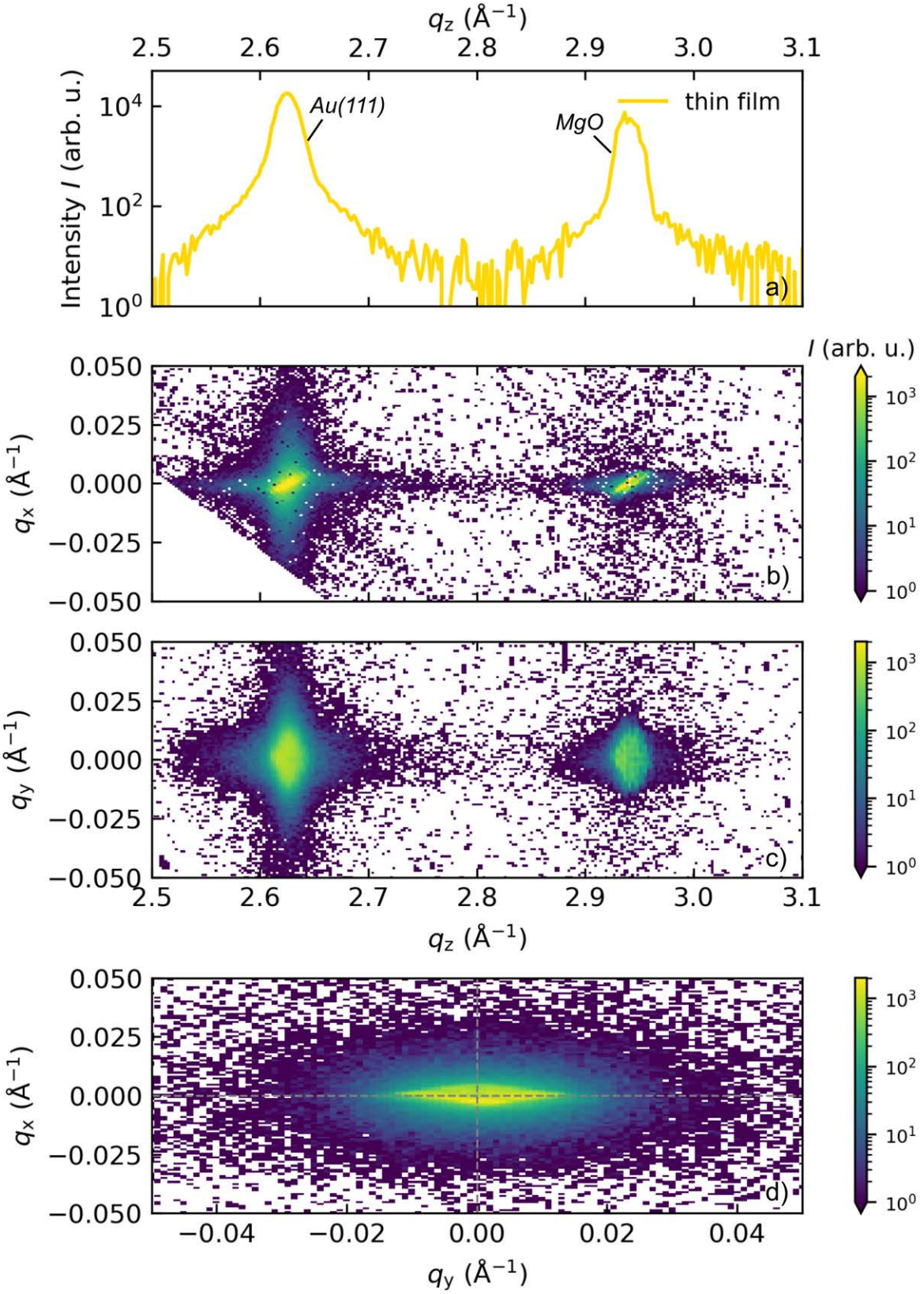

Figure 6: Subsets of the three-dimensional reciprocal space of the gold thin film. **a)** Peak intensities integrated over the in-plane axes q_x and q_y. The MgO reflection (right) exhibits a similar brightness as the Au (111) reflection (left). Reading the q_z-value of the gold maxima from the RSM, the lattice constant is calculated to 4.154 Å. **b)-d)** q_x-q_z, q_y-q_z, and q_x-q_y projections of the reciprocal space showing the sample and substrate peak.

5.2 Gold Nanocubes

The same subset of the three-dimensional reciprocal space of the AuNCs is visualized in fig. 8. The q_x-q_z and q_y-q_z maps reveal three maxima at different q_z-coordinates. The first comparatively dim maximum at q_z= 2.61 Å^{-1} relates to the Au (111) reflection. The bright maximum in the middle, at q_z = 3.04 Å^{-1}, relates to the MgO substrate peak and the maximum on the right side of the RSM, at q_z = 2.94 Å^{-1}, to the Au (002) peak. The center points of the MgO and Au (002) peaks possess almost the same intensity as demonstrated in the integrated intensity as function of q_z in fig. 8a). The substrate peak is broadened along the q_z-axis because of the finite layer thickness, and hence, finite number of scattering layers, and, moreover, because of the angular convergence and spectral width of the X-ray source.

Both the Au (002) and Au (111) are broadened along the q_x- and q_y-axis. The general curvature and broadening can be attributed to the mosaicity of the sample, as it is made up of numerous 180 nm nanoparticles and resembles a powder. Therefore, the appearance of sections of Debye-Scherrer rings is in line with what is expected for such a sample. In fig. 8d), in the q_x-q_y dimension, only one bright spot around the center pixel can be seen where all three maxima lie above each other combining into two peaks. Fig. 7 visualizes the slight change of the scattering vector in q_x, due to the tilting of the nanocubes relative to each other, causing the Bragg peak to be elongated in this direction. In a similar way, the rotation of the nanocubes around the surface normal causes broadening in the q_y-dimension.

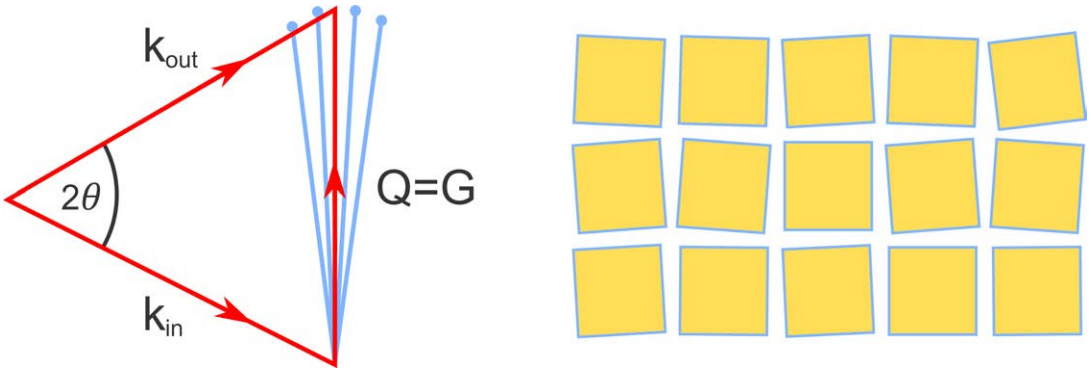

Figure 7: Due to the tilting of the nanocubes relative to each other, the reciprocal space vector $\vec{G}$ shifts in the in-plane q_x- and q_y-directions, causing the Bragg peak to broaden in these directions in reciprocal space. Adapted from [35].

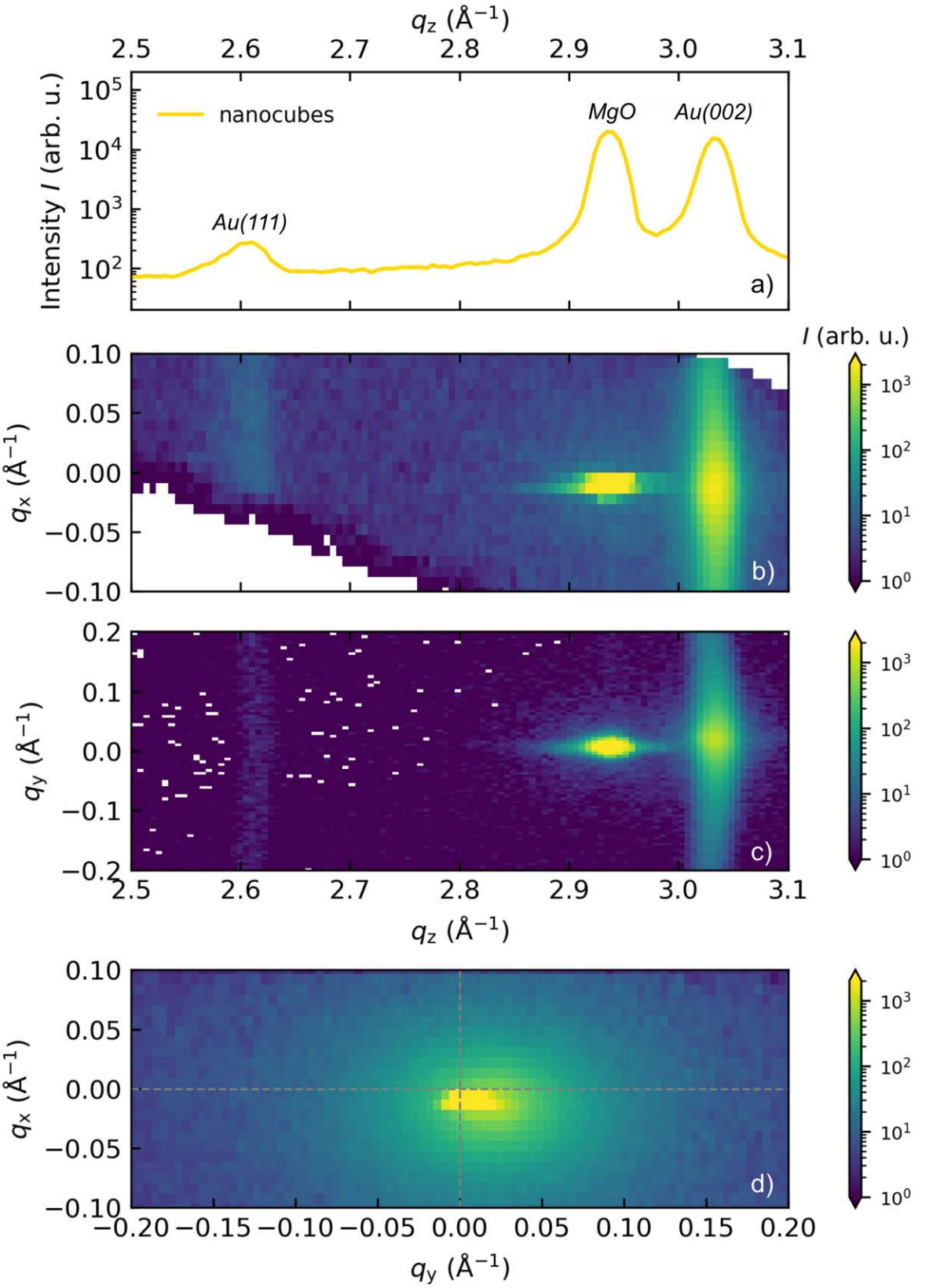

Figure 8: Three-dimensional reciprocal space of the AuNC sample depicted as projections in the q_x-q_z, q_y-q_z, and q_x-q_y space. **a)** Integrated intensity along q_y and q_x versus the q_z-coordinate showing three local maxima relating to the Au (111), MgO, and Au (002) Bragg peaks. The Au (002) and MgO maxima appear much brighter than the Au (111) maximum. $I(q_z)$ encodes the average out-of-plane lattice constant d_3 of the diffracting layers by the center position of their Bragg peaks. **b)-d)** q_x-q_z, q_y-q_z, and q_x-q_y projections of the reciprocal space, showing the two sample and one substrate peak. In d) only two overlapping maxima are observed.

Repeating the calculations from the previous section, the lattice constants of Au (002) and Au (111) amount to:

$$\text{Au (111):} \quad a = \frac{2\pi}{q_z}\sqrt{1^2+1^2+1^2} = \frac{2\pi}{2.61\,\text{Å}^{-1}} \cdot \sqrt{3} = 4.17\,\text{Å}, \tag{12}$$

$$\text{Au (002):} \quad a = \frac{2\pi}{q_z}\sqrt{0^2+0^2+2^2} = \frac{2\pi}{3.04\,\text{Å}^{-1}} \cdot 2 = 4.13\,\text{Å}. \tag{13}$$

Both peak positions result in a similar lattice constant, which is, again, close to the bulk-gold literature value of 4.07 Å.

From this measurement, important structural details can be deduced, namely the fact that the AuNCs preferentially grow in the Au (002) orientation with a small contribution of the Au (111) orientation. Most likely, the majority of the cubes are oriented in the Au (002) orientation and a small portion are tilted relative to the substrate and, thus, appear as the Au (111) contribution. Furthermore, the Au (002) reflection exhibits a local maximum around the q_x-q_y center pixel, indicating an overall higher crystallinity or order of the crystal lattice, most likely due to the cubes themselves being distributed quite ordered on the substrate. The SEM in fig. 2 underlines this assumption, since the cubes can be seen being aligned quite well next to each other.

5.3 L-Chiral Gold Nanocubes

The RSM in fig. 9 of the l-chiral AuNCs displays a similar result to the AuNCs as the same three Bragg peaks at the same q_z-positions are visible. The integrated intensity $I(q_z)$ in fig. 9a) reveals that the Au (111) and Au (002) reflections display about the same brightness, from which we know that both crystal directions occur about equally in the sample compared to the AuNCs where the Au (002) reflection dominates the Au (111). Another factor that influences the brightness is the crystal quality, implying that the AuNC sample exhibits a higher order of crystallinity. Formally, the intensity of a reflection is defined to be proportional to the scattering volume and the structure factor, as previously described by eq. (6).

Similar to the AuNCs, both gold peaks are broadened along q_x and q_y in fractions of Debye-Scherrer rings, which, again, is to be expected due to the small size and powder-like nature of the nanocubes. The white "spots" in the RSM are simply reciprocal space vectors where no photons have been scattered or detected. Since the estimated q_z-coordinates are the same as for the AuNCs, the calculated lattice constant remains in the region of the expected result for bulk gold.

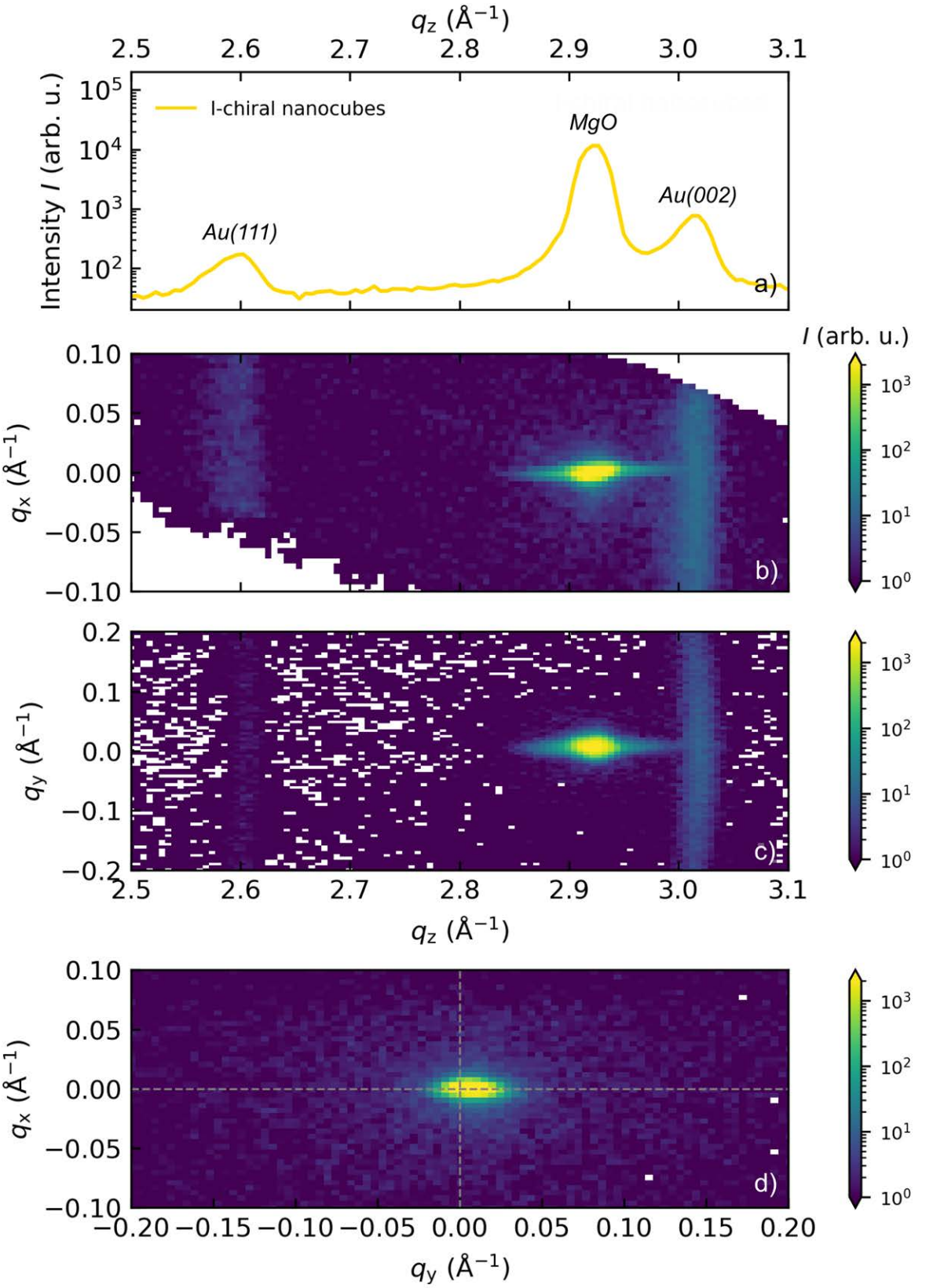

Figure 9: Three-dimensional reciprocal space of the nanocube sample depicted as projections in the q_x-q_z, q_y-q_z, and q_x-q_y space. **a)** Integrated intensity along q_y and q_x versus the q_z coordinate depicting three local maxima relating to the Au (111), MgO, and Au (002) Bragg peaks from left to right. The MgO maximum appears much brighter than the Au (111) and Au (002) reflections. **b)-d)** q_x-q_z, q_y-q_z, and q_x-q_y projections of the reciprocal space showing the two sample peaks and one substrate peak. In d) only two overlapping maximum are observed.

6 Discussion of the Static XRD Measurements

To summarize, the AuNCs reveal three Bragg reflections, two sample reflections, and one substrate reflection. Both Au (002) and the MgO substrate peak are much brighter than the Au (111) peak.

The l-chiral AuNCs reveal a similar result, differing only in the relative intensities of the Bragg reflections. Both gold peaks exhibit a similar brightness, leading to the conclusion that about half of the cubes are oriented parallel to the substrate layer and half are tilted or rotated. This can be explained by the fact that the cubes are grown in a solution and then deposited on the substrate in partially random orientations (as described in section 4.1), leading to the appearance of partial Debye-Scherrer rings in reciprocal space.

The overall more disordered orientation of the LAuNCs compared to the AuNCs can be seen in the SEM imaging in fig. 2. The gold thin film reveals a single, bright, and narrow Au (111) reflection next to the substrate reflection, indicating a higher order of crystallinity. The sample reflection possesses a broad and narrow portion, implying that the sample has two subsections with different morphologies, one of higher order and one with more defects.

6.1 Structure-Factor Analysis

To analyze the observed intensities of the individual maxima, a discussion of the contributing factors, namely the scattering factor and the lattice sum, is needed. In general, the scattering amplitude is defined via eq. (6). Neglecting the lattice sum, only the structure factor is considered for now. The reciprocal lattice vector $\vec{G}$ can be expressed in terms of the Miller indices (hkl) and the structure factor can now be written as:

$$S = S_{hkl} = \sum_{n=1}^{N} f_{\mathrm{Au}} e^{-i\vec{G}_{hkl}\cdot\vec{r}_n} \tag{14}$$

where f_{Au} is the atomic form factor of gold. The reciprocal lattice vector is defined by:

$$\vec{G}_{hkl} = \frac{2\pi}{a}(hx_n + ky_n + lz_n) \tag{15}$$

where x_n, y_n and z_n are the components of the reciprocal basis vectors $\vec{r}_n$. The reciprocal basis vectors $\vec{r}_n$ for a fcc lattice are:

$$\begin{aligned}
\vec{r}_0 &= (0,0,0),\\
\vec{r}_1 &= \frac{a}{2}(\hat{y}+\hat{z}) = \frac{a}{2}(0,1,1),\\
\vec{r}_2 &= \frac{a}{2}(\hat{x}+\hat{z}) = \frac{a}{2}(1,0,1),\\
\vec{r}_3 &= \frac{a}{2}(\hat{x}+\hat{y}) = \frac{a}{2}(1,1,0).
\end{aligned} \tag{16}$$

Simplifying the expression for the structure factor thus leads to:

$$S_{hkl} = f_{\mathrm{Au}}[1 + e^{-i\pi(h+k)} + e^{-i\pi(h+l)+e^{-i\pi(k+l)}}]. \tag{17}$$

Performing this calculation for each of the observed gold reflections yields:

$$
\begin{aligned}
S_{111} &= f_{\mathrm{Au}}[1 + e^{-i2\pi} + e^{-i2\pi} + e^{-i2\pi}] = 4f_{\mathrm{Au}} \\
\mathrm{S}_{002} &= f_{\mathrm{Au}}[1 + e^{0} + e^{-i2\pi} + e^{-i2\pi}] = 4f_{\mathrm{Au}}, \\
\mathrm{S}_{001} &= f_{\mathrm{Au}}[1 + e^{0} - i2\pi + e^{-i\pi} + e^{-i\pi}] = 0.
\end{aligned}
\tag{18}
$$

While the structure factors of the Au (002) and Au (111) reflections are equal to $4f_{\mathrm{Au}}$, it can be additionally shown that the Au(001) reflection is forbidden purely because its structure factor and, therefore, its intensity is vanishing. This calculation indicates that the intensity differences between the different sample reflections in the RSMs do not originate from one of the crystal orientations scattering more efficiently, but from different amounts of the respective orientations being present in the sample, i.e., from differing lattice sums.

6.2 Conclusion

In conclusion, the static diffraction experiments provide us with a greater understanding of the samples' morphologies by supplying information on in-plane and out-of-plane features through the shape, intensity, and position of the Bragg reflections in the reciprocal spaces. From the overall appearance of the RSMs, one can gain a good understanding of the samples' morphologies, which was then followed by an analysis of the respective structure factors. It was found that the thin film exhibits a twofold Au (111) reflection, with a narrow and broad contribution, indicating two regions of differing morphology within the layer. In contrast, both nanostructured samples exhibit Au (111) and Au (002) reflections in partial Debye-Scherrer rings, implying polycrystallinity through random orientation of the nanocubes. Both Au (002) reflections are brighter than the Au (111) ones, even exhibiting a local maximum for the AuNCs, indicating a large number of lattice planes being oriented in the Au (002) direction. A structure-factor analysis verified that the differing lattice sums, and not different structure factors, are responsible for the peak intensities observed in the RSMs in figs. 6, 8, and 9.

This analysis lays the foundation for the next chapter, in which the ultrafast strain response of the three samples after laser excitation will be compared and discussed, since for these measurements the exact q_z-coordinates are necessary information.

7 Ultrafast Strain Dynamics of Gold Nanoparticles

In this section, the results of the static XRD measurements will be further investigated by employing time resolved measurement techniques. Firstly, the general idea of the time-resolved "pump-probe" technique will be explained, followed by a theoretical analysis of what results and dynamics can be expected from the gold samples and an explanation of the used measurement techniques and setup. After presenting the measurement results, they will be qualitatively compared and discussed in terms of calculating the quasi-static temperature increase in the samples after laser-excitation with different approaches. Lastly, possible explanations for the found results and differences between the nanostructured and continuous samples will be discussed.

7.1 Ultrafast Dynamics in Solids

One fundamental question to answer is how to resolve strain dynamics on the ultrafast, meaning pico- to femtosecond timescale, as processes faster than 100 ps cannot be resolved by standard electronics [41]. A solution for this is presented by using pump-probe spectroscopy and, in particular, for resolving ultrafast strain dynamics, by utilizing ultrafast X-ray diffraction (UXRD). UXRD is an effective technique for quantifying the lattice dynamics in solids with femtosecond time resolution, combining the nanoscale resolution capabilities of XRD and the ultrafast time-resolution capabilities of pump-probe techniques.

However, before investigating the experimental results, it is important to understand how the light-matter interaction and subsequent lattice dynamics at the nanoscale work and what the main working principles of UXRD encompass.

7.1.1 Pump-Probe Spectroscopy

The basic principle of pump-probe spectroscopy includes exciting a sample with short pump pulses and triggering changes in the sample's properties. A delayed short probe pulse then detects pump-pulse-induced changes in the sample. By varying the timing between the pump and probe pulse, one can record a temporal evolution of the induced changes in a sample. The time resolution is mainly determined by the length of the pulses [41].

However, it is important to note that the processes or dynamics of interest have to follow certain rules before being able to be resolved with the pump-probe technique [39]. Firstly, the dynamics induced in the sample need to be reversible so that the same process can be recorded many times for each of the different delays between pump and probe without inflicting damage to the sample. This also includes that the sample needs to be able to relax back to its initial state before the following excitation. Furthermore, the pump and probe pulses need to be considerably shorter than the dynamics they try to resolve and they need to be spatially and temporally synchronized relative to one another. In the here presented experiments, a type of pump-probe spectroscopy called ultrafast X-ray diffraction (UXRD) will be employed in order to examine the ultrafast lattice dynamics in the gold samples, specifically, the temporal evolution of the average out-of-plane lattice spacing after laser-excitation. In UXRD, the pump pulse consists of a 35 fs near-infrared laser with a center wavelength of 800 nm while the probe consists of about 250 fs long CuK_α X-ray pulses with a wavelength of 1.54 Å. X-rays are used, for one, to measure the lattice constant and on the other hand because they possess a large penetration depth of a few micrometers regardless of the optical properties of the sample [39, 41]. A schematic depiction of the technique can be seen in fig. 10.

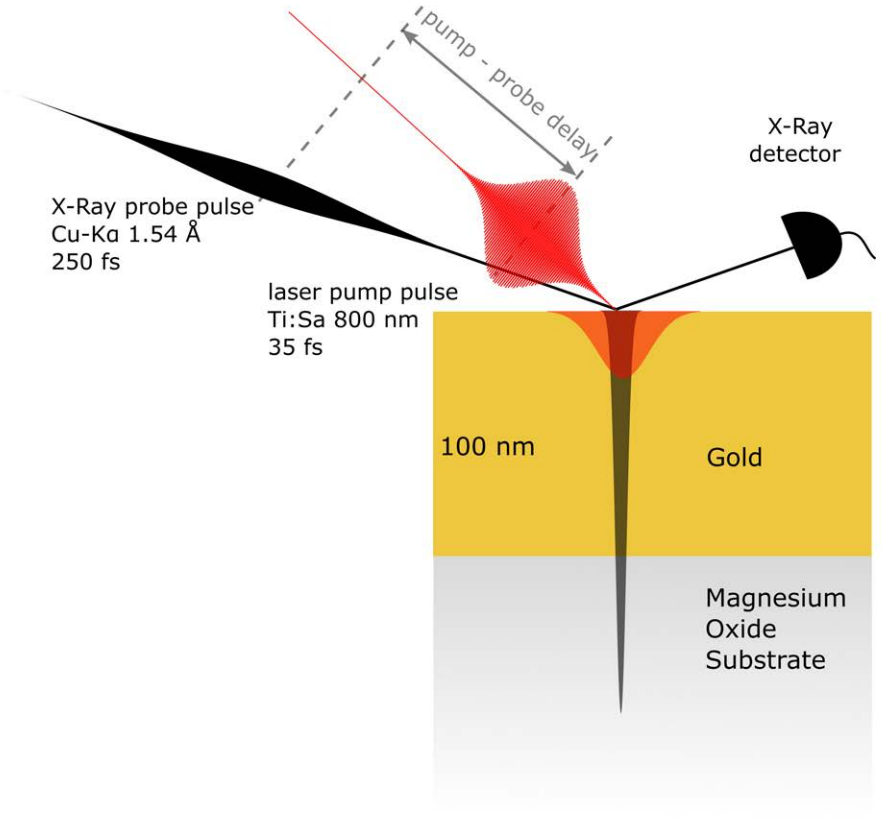

Figure 10: Schematic depiction of the pump-probe technique. A 35 fs laser pump pulse excites the sample and changes its lattice. The out-of-plane lattice change is detected by a time-delayed 250 fs X-ray probe pulse. The sketch is adapted from [39].

7.1.2 Picosecond Ultrasonics with UXRD

In general, picosecond ultrasonic experiments, in particular UXRD, can extract the transient strain response of samples such as gold and AuNCs to laser-excitation from the shift of the Bragg peaks along q_z in reciprocal space that originates from the lattice structure changing. A detailed description of picosecond ultrasonics is given by *M. Mattern et al.* [11]. Here, the general principle is summarized.

The energy deposited by an optical pump pulse creates a thermoelastic stress profile in the material that creates a localized strain response, consisting of a propagating strain pulse and a quasi-static thermal expansion that propagates via heat diffusion, two processes that are associated with different time scales. For the samples investigated in this thesis, the strain wave propagation is mainly observed in the first couple 100 ps, the quasi-static thermal expansion or quasi-static strain dominates afterwards up to several nanoseconds. In general, the time T it takes for a strain pulse to propagate through the sample and back to the surface is given by $T = d/v_s$ where d denotes the film thickness and v_s the speed of sound. Heat diffusion, on the other hand, is proportional to the square of the film thickness ($T_{\text{diff}} \propto d^2$). Since X-ray diffraction is layer-specific and the strain response causes localized lattice distortions, UXRD is the right approach.

The observable Bragg-peak shift is a linear measure of the introduced energy density, as it is proportional to the average strain of the lattice [11]. Formally, UXRD measures the time-dependent and layer-specific

strain $\eta(t)$, since the transient shift of the Bragg peaks along q_z directly relates to the transient out-of-plane lattice spacing $d_3(t)$ [11]:

$$\eta(t) = \frac{q_z(t) - q_z(t_0)}{q_z(t_0)} = -\frac{d_3(t_0) - d_3(t)}{d_3(t_0)} \tag{19}$$

where $q_z(t_0)$ denotes the peak position and $d_3(t_0)$ the out-of-plane lattice spacing before excitation, and $q_z(t)$ the peak position and $d_3(t)$ the out-of-plane lattice spacing at delay t after excitation, respectively.

The only difference to the static setup described in section 4.4 is given by the now introduced 800 nm pump laser, whose time delay, relative to the X-ray pulses, is set by the length of the delay stage.

After introducing UXRD and its main principles, it is important to understand the response of metals, such as gold, at a nanoscopic scale to later understand the transient strain evolutions seen in figs. 17-19.

On ultrafast timescales, a commonly used approach is to view the electrons and phonons as coupled heat baths or different degrees of freedom that contribute separately to the observed strain in a sample [11, 44]. Exciting one of the subsystems, e.g., via a laser pulse, subsequently leads to energy transfer to the other, to equalize their temperatures. The amount of energy that each subsystem can store, with respect to its temperature, is given by their respective heat capacity. This distinction between subsystems is formally described by the Grüneisen approach, which relates the energy deposited in each subsystem to the resulting stress contributions that ultimately drive the strain response. Consequently, the quasi-static strain we observe is a linear measure of the stress contributions of each subsystem, which in turn, are proportional to their respective energy densities. For the subsystem i the associated external stress σ_i can be expressed as [11]:

$$\sigma_i^{\text{ext}} = \Gamma_i \rho_i \tag{20}$$

where Γ_i is the Grüneisen-parameter that encodes how efficiently each energy density ρ_i generates strain. In UXRD experiments, the near-infrared pump pulse deposits a large amount of energy in the upper few nanometers of the sample where it is predominantly absorbed by the electrons. These hot electrons equilibrate almost instantly throughout the entire sample and subsequently transfer their energy to the phonons by scattering. The rate of this transfer is dictated by the material-specific electron-phonon-coupling strength g_{ep}, which, for gold, is comparably weak, and the electronic heat capacity C_{e}. The electron-phonon equilibrium is established in 1-5 ps [8], with the equilibrium time τ being proportional to g_{ep}/C_e.

Heating the electron and phonon system induces a local lattice expansion, or in other words, strain. Furthermore, the sudden increase in energy density at the surface layer of the sample generates a strain pulse that propagates into the bulk of the sample at the speed of sound. Since the pulse originates at the surface, the local expansion of the lattice leads to compression of the adjacent lattice, and thus, the strain pulse is of bipolar nature. The order, in which the processes take place, can be seen in fig. 11. The propagation and reflection of the strain wave at interfaces can be described by a linear chain model where the masses represent the individual atoms and the springs the interatomic bonds. Following Hook's law, the force exerted on the system leads to displacement of the masses from their equilibrium positions and the rest of the system answers by following the original displacement, pulling and pushing on neighboring masses. This external stress causes deformation of the solid and the resulting atomic displacement defines the strain [11].

As mentioned, the total strain response is a superposition of two processes associated with different time scales. The coherent acoustic phonon interference, or in other words, the strain pulse propagation, dominates in the first couple hundred picoseconds after laser-excitation and causes local and transient lattice distortions, which manifest themselves as an oscillation of the measured strain amplitude. In contrast,

the quasi-static thermal expansion of the lattice is associated with a slow increase of the measured strain amplitude over several nanoseconds and is caused by thermal diffusion.

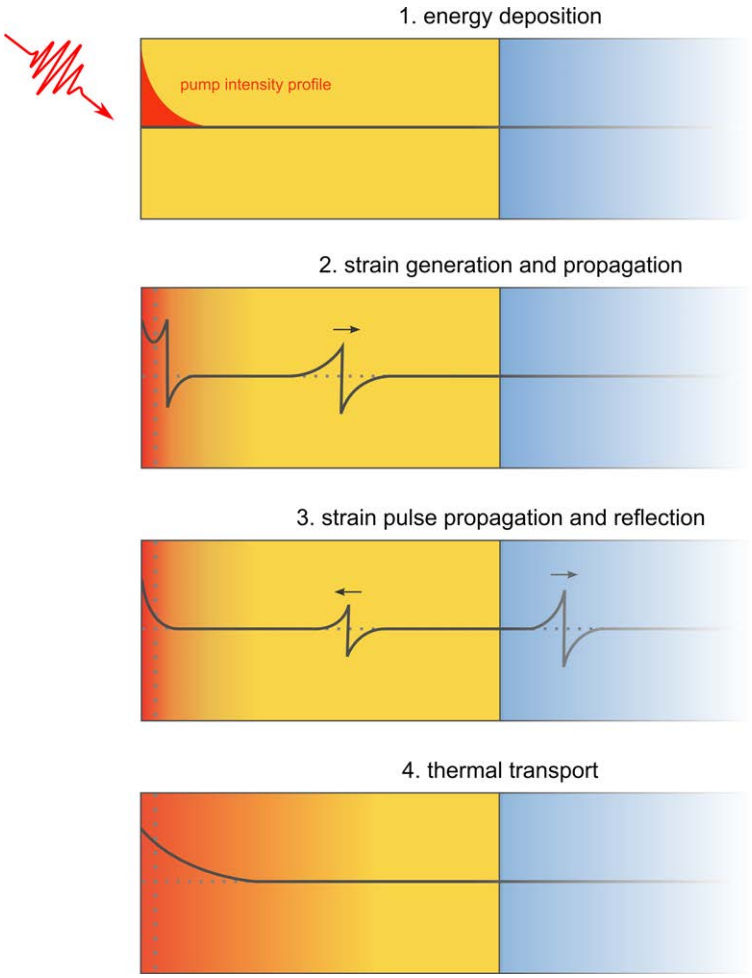

Figure 11: Series of events after laser excitation of a metal thin film. The energy deposited by the pump pulse creates a stress profile at the surface of the sample. A bipolar strain pulse is launched and propagates through the bulk with the speed of sound. When reflection occurs at an interface, due to an impedance mismatch, the sign of the strain pulse changes. Finally, after the strain pulses have propagated out of the medium, the quasi-static thermal expansion concludes the picosecond strain response. The schematic is adapted from [11].

As the strain wave propagates through the bulk, it loses amplitude, due to interaction with lattice defects, an effect characterized by the coherence length. At interfaces, e.g., between the metallic transducer and the substrate, the wave can be partially reflected or transmitted based on the acoustic impedance difference between the neighboring layers. The acoustic impedance of a material is given by its mass density ρ_m and the sound velocity v_s [11]

$$Z = \rho_m v_s. \tag{21}$$

The acoustic reflection coefficient R is defined as:

$$R = \frac{Z_2 - Z_1}{Z_1 + Z_2}. \tag{22}$$

Thus, reflection occurs whenever the acoustic impedance of the two media differ ($Z_1 \neq Z_2$). If $Z_1 > Z_2$, the reflected wave's amplitude undergoes a sign change, corresponding to a phase shift of 180°. If $Z_1 < Z_2$, no sign change or phase shift takes place. Furthermore, the response of the solid includes

Poisson contributions, which, however, will be discussed in the context of the measurement results in section 9.

7.2 Experimental Setup for UXRD

The setup for time-resolved measurements is similar to the setup used for static measurements and differs only through the inclusion of a pump setup and the necessity of pulsed X-rays. The latter are generated by a plasma based X-ray source (PXS). For evaluating the temporal evolution of the strain, a method called Reciprocal Space Slicing is employed [38].

The setup used to realize the time-revolved measurements can be seen in fig. 12. The setup is described in detail in the master's thesis of *J.-E. Pudell* [41] and will be summarized here. The pump laser is generated by the oscillator laser Mantis that uses a titanium doped sapphire (Ti:Sa) crystal as its active medium. The ultrashort pulses or mode-locking of the laser is achieved via a Kerr-lense in a designated resonator. The oscillator emits 40 fs long pulses with an energy of 5 nJ per pulse and a center wavelength of 800 nm at a repetition rate of 80 MHz.

Following the initial creation, the laser pulses have an output power of 400 mW and have to be further amplified by the two-stage Ti:Sa amplifier system Legend Elite duo that uses chirped pulse amplification to increase the output power to 8 W. Chirped pulse amplification is a technique that allows for further amplification of lasers without damaging the gain medium and was introduced by *D. Strickland and G. Mourou* [45] for which they earned a Nobel prize in 2018. The pulses are stretched in time to 150 ps via a grating stretcher and are amplified in a regenerative cavity that uses a Ti:Sa crystal as its gain medium, which in turn is pumped by an Evolution HE pump laser. Pockels cells are used for coupling of the laser pulses into and out of the cavity. Before exiting, the light travels trough a second booster amplifier that also uses a Ti:Sa-crystal as its gain medium that, again, is pumped by the Evolution HE pump laser. Finally, the pulses are compressed in time to 35 fs in a grating compressor and exit the amplifying setup.

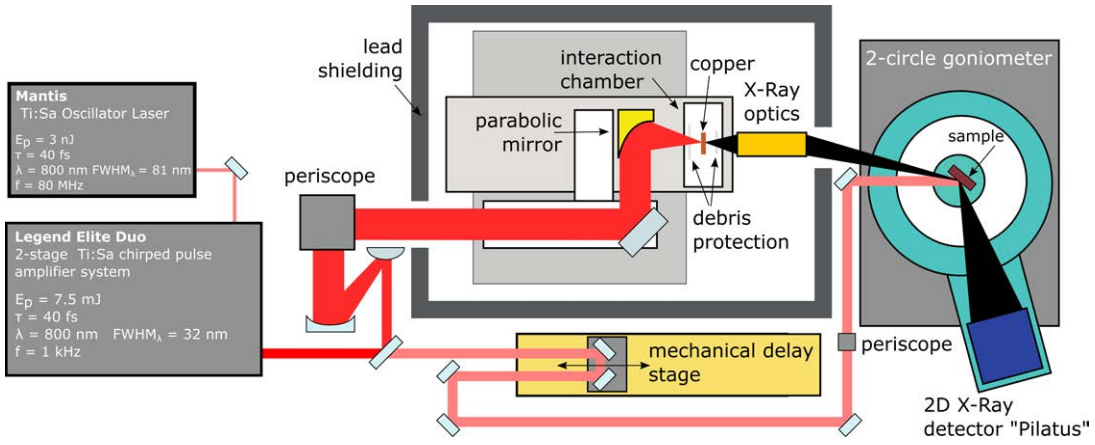

Figure 12: Top view sketch of the UXRD setup. The 800 nm pump laser is generated by the oscillator laser Mantis and further amplified by the two-stage Ti:Sa amplifier system Legend Elite duo that uses chirped pulse amplification to increase the output power to 8 W. The pump laser currently has a pulse energy of 7.5 mJ, a duration of 35 fs and a repetition rate of 1 kHz. Utilizing a beam splitter, about 95 % of the pulse energy is split off and focused onto a copper foil in the plasma X-ray source to generate the X-rays. The Montel multilayer optic focuses the CuK_α-part of the spectrum (the probe pulse) onto the sample. The remaining 5 % of the pulse energy is directed over a mechanical delay stage and focused onto the sample as well. By changing the length of the delay stage, the time delay between pump and probe is set. An area detector on the outer circle of the goniometer detects the diffracted photons. The schematic is taken from [39].

The now amplified pulses are split by a beam splitter so that 95 % are used for generating the pulsed X-rays and the remaining 5 % are used for exciting the sample after traversing a mechanical delay stage. Its length determines the timing between the pump and probe pulses. The longer the delay path of the laser, the larger the time delay between pump and probe. The fluence, under which the pump pulses are incident on the sample, can be adjusted by changing the orientation of a $\lambda/2$-waveplate relative to a polarizer in the beam path. Since the waveplate introduces s-polarized components to the laser's electrical field, a polarizer has to be used to filter these components so that only the p-polarized components remain. To stabilize the beam position, a small part of the pump-laser is transmitted through the backside of a polished mirror onto a CCD-camera. If the beam's position changes, an active steering motor corrects the deviation and ensures that the excitation spot on the sample stays the same during the course of a measurement.

The probe pulses are generated by focusing the remaining laser energy via a periscope and a parabolic mirror onto a 15 µm thin copper tape. The large electric field of the laser frees the weakly-bound valence electrons of the copper, creating a plasma of free electrons that is accelerated away from the metal. When the electric field changes its sign, the electrons are accelerated back again and collide with the metal, creating X-rays in the process. The copper tape is constantly moved via a spool setup so that each laser pulse hits a fresh piece of the copper surface. Because copper debris is generated in the process, transparent plastic bands are placed in front of and behind the copper tape, in order to protect the entrance and exit windows of the PXS (fig. 13).

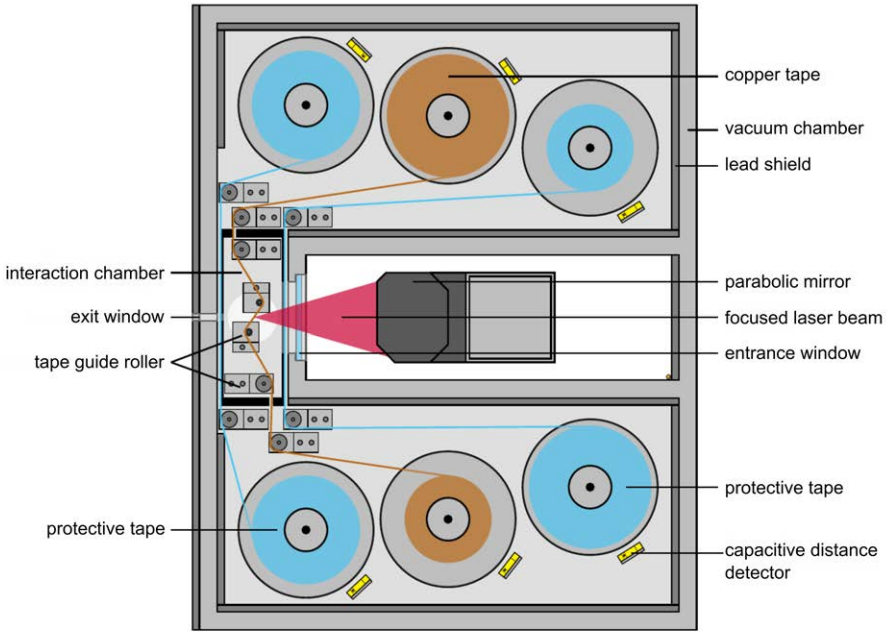

Figure 13: PXS setup. The laser pulses are focused onto a copper tape, which is continuously moved via the spool system so that each laser pulse hits a fresh target. To protect the entrance and exit windows of the interaction chamber from copper debris, protection plastic bands run concurrent to the copper band. The entire setup is encased in a vacuum chamber with lead shielding on the outside. The schematic is taken and translated from ref. [41].

The X-ray pulses have a duration of 250 fs [39]. The CuK_α part of the emitted spectrum is then focused by a Montel multilayer optic (fig. 12) onto the sample where they are diffracted. To provide a reference for the incident photon flux, the X-ray's intensities are monitored via an X-ray intensity detector. Finally, after being diffracted, a position-sensitive area detector counts the incident photons. The data evaluation routine that transforms the detector's data from real space to reciprocal space is the same as the one that has been used for the static measurements, and is described in section 4.4.

Before commencing with the strain measurements, the spatial overlap of the pump and probe pulse and the delay-stage position for time-zero, where pump and probe are simultaneously incident on the sample, have to be determined. An in-depth explanation of the determination of time-zero via the near-instant ultrafast strain-response of a metal-insulator superlattice is given in references [39, 41, 46]. Instead of generating a full RSM and determining the diffraction maxima's position for every delay time between the pump and probe pulses to measure the temporal evolution of the out-of-plane lattice spacing, a more efficient evaluation method called Reciprocal Space Slicing is used.

Data Processing with Reciprocal Space Slicing

The experimental technique of Reciprocal Space Slicing (RSS) was developed by *S. P. Zeuschner et al.* in 2022 and is explained in detail in the publications [38, 40].

Instead of determining the q_z-position of the Bragg peak before and after laser-excitation by measuring a full RSM for every diffraction angle combination, and thus, calculating the corresponding strain, RSS requires only one slice of the reciprocal space that has been mapped with an area detector at one incident diffraction angle α_{in}. Since the area detector already records diffraction maxima with different α_{out}-angles for one fixed α_{in}-position and the Bragg peaks can be assumed to only shift along the q_z-coordinate after laser excitation, examining a one-dimensional subset or slice of the full reciprocal space is sufficient to analyze the transient strain. The α_{in}-position has to be chosen so that the Bragg-peak's intensity maximum occurs on the center pixel of the detector, which can be approximated by a straight line in reciprocal space. The shift $\Delta q_{z,\mathrm{RSM}}$ of a Bragg peak, resulting from the change of the out-of-plane lattice spacing, is closely related to its projection $\Delta q_{z,\mathrm{RSS}}$ in the reciprocal space slice. Thus, the strain is given by the projection of the RSM and relates to the shift of the RSS on the detector via a scaling factor s:

$$\eta_{\mathrm{RSM}} = -\frac{\Delta q_{z,\mathrm{RSM}}}{q_{z,0}} = -\frac{\Delta q_{z,\mathrm{RSS}}}{q_{z,0}} \left(1 + \left(\frac{w_z}{w_x}\right)^2 \tan^2\left(\theta_{\mathrm{B}}\right)\right) = -\frac{\Delta q_{z,\mathrm{RSS}}}{q_{z,0}} \cdot s. \tag{23}$$

w_z and w_x denote the width of the Bragg peak along the respective reciprocal space coordinates q_z and q_x. For symmetrical scattering conditions, the angle θ_{B} corresponds to the chosen incident angle α_{in}. The optimal α_{in}-angles have been chosen from the static measurement results from the previous section 4.4. A sketch of the RSS scheme can be seen in fig. 14.

For the evaluation of the measured time-resolved data, this technique was employed. After transforming the detector images into reciprocal space as previously described, a one-dimensional intensity map $I(q_z)$ was generated for each delay step. The recorded intensity maxima are fitted with a Gaussian function and a linear background correction. From the center position of the Gaussian, the q_z-coordinate is determined, which corresponds to the out-of-plane lattice spacing. For the here recorded measurements, the scaling factor between $\Delta q_{z,\mathrm{RSM}}$ and $\Delta q_{z,\mathrm{RSS}}$ was set to be 1 because of the previously observed very large broadening of the peaks along the q_x- and q_y-coordinates.

To calculate the shift of a peak, the transient q_z-position is subtracted from a reference position before laser excitation so that any change from the initial peak position can be attributed to laser-induced strain. From the shift of q_z, the strain was calculated via eq. (19).

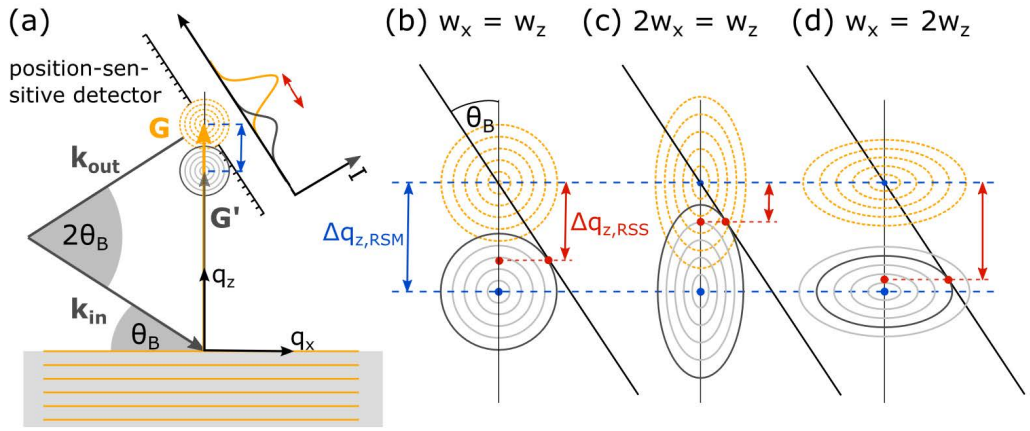

Figure 14: a) Schematic depiction of the RSS-technique during the standard diffraction situation. The technique exploits that the area detector probes multiple α_{out} at the same time for one fixed α_{in} and since the Bragg peaks are assumed to only shift along q_z, the subset of the reciprocal space detected by the stationary PSD is sufficient to measure the change. In the schematic, the PSD is depicted as the straight line cutting through the center of the Bragg peaks. The shift along this detector line is proportional to the shifting along q_z via a scaling factor s. **b)** Ratio between $\Delta q_{z,\text{RSS}}$ and $\Delta q_{z,\text{RSM}}$ for different size Bragg peaks. For peaks broadened along q_x, the scaling factor is close to 1. The figure is taken from [11].

For positive strain-values the peak moves to smaller q_z-values, which is the case depicted in fig. 15. Here, the fit of a peak before time-zero or excitation is shown as a continuous red line. After 79 ps, the peak has shifted towards smaller q_z-values and the corresponding fit function is now depicted as a dotted black line.

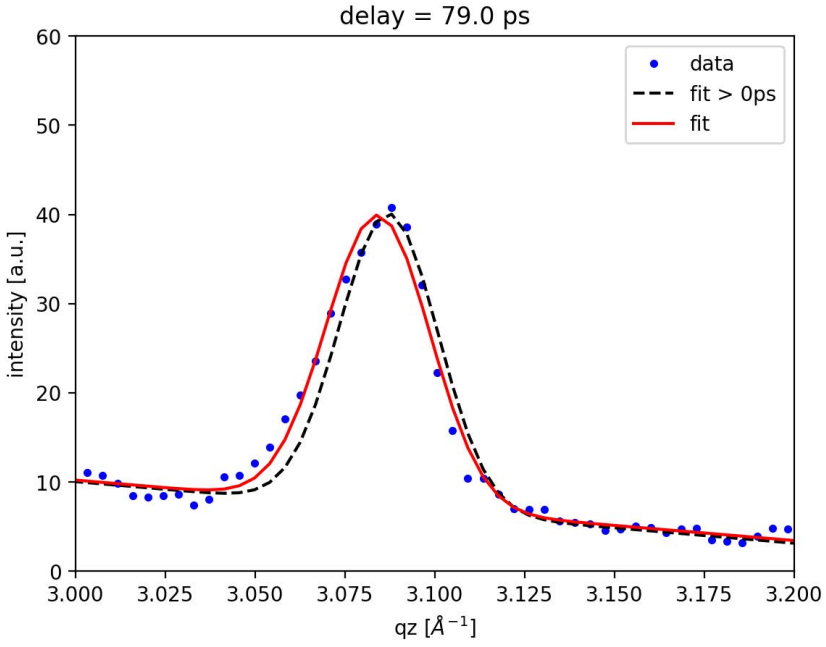

Figure 15: Example of the Gaussian fit before and 79 ps after excitation. The red fit represents the reference peak position before excitation, the dotted black line, corresponding to the blue data points, the fitted peak position after. As the sample is excited, the lattice spacing increases and the peak shifts to smaller q_z-values.

7.3 Interpreting UXRD Signals

During UXRD measurements, the observed Bragg reflections can change due to a multitude of reasons (summarized in fig. 16). If any kind of change or distortion is introduced by the pump laser into the lattice structure, the observed diffraction signal will react accordingly. A detailed explanation of the influencing factors is given in the dissertation of *A. von Reppert* [47] and by *M. Bargheer et al.* [48]. Here, a short summary is presented.

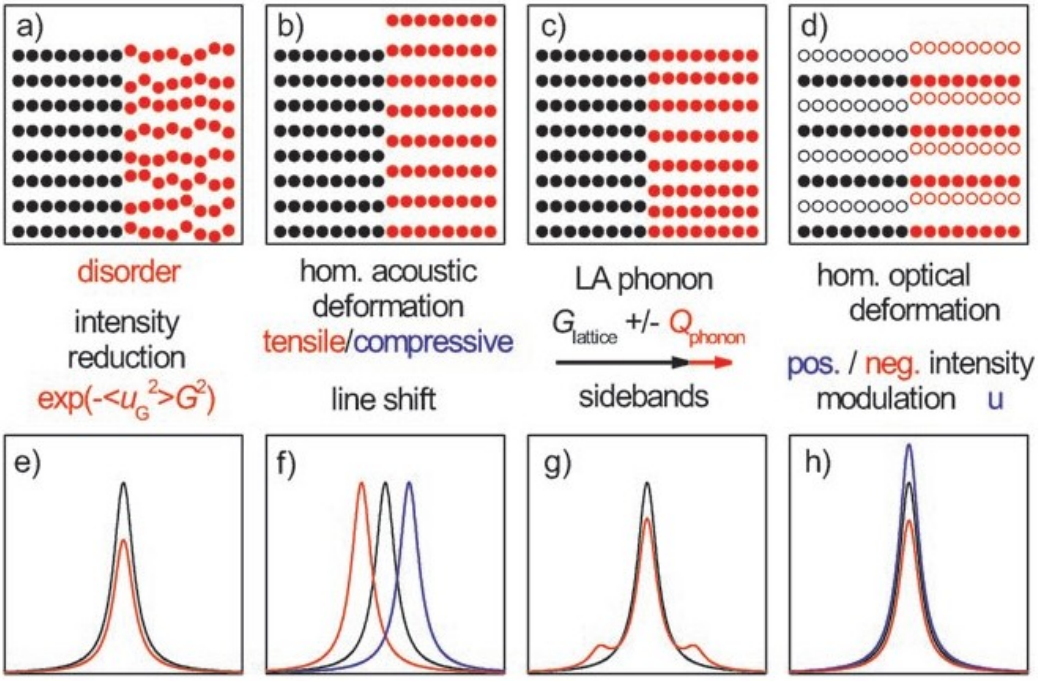

Figure 16: Bragg peaks changing due to varying types of lattice distortions. **a)- d)** Schematic depiction of the original lattice spacing (black) and distorted lattice (red). **e)- h)** Resulting change of the Bragg peak. The original peak is depicted in black and the peak resulting from the lattice distortion is depicted in red and blue. The figure is taken from [48].

For a random displacement of the individual atoms, due to thermal motion, the observed signal decreases in intensity according to the Debye-Waller factor $e^{-<u_g^2>G^2}$. For larger temperatures, the incoherent statistical movement of the atoms increases, and thus, the intensity decreases further. $< u_g^2 >$ describes the average squared deviation of the atom's position along $\vec{G}$.

Homogeneous longitudinal acoustic deformation of the lattice leads to the average distance between the lattice planes increasing or decreasing. While the intensity of the peak does not change, it will shift to smaller or larger diffraction angles. In time-resolved measurements, this shifting of the peaks after laser-excitation can be observed on a time scale of a few hundreds of femtoseconds to nanoseconds and will be the main focus of the data analysis, since it is directly related to the out-of-plane lattice spacing [11].

The periodic modulation of the lattice spacing by longitudinal acoustic phonons generates sidebands in the observed signal, since the phonons' momentum $\vec{Q}$ is added or subtracted from the reciprocal lattice vector $\vec{G}$ to uphold momentum conservation during the scattering process.

Optical phonons cause internal distortions of the unit cell and, thus, a change in the structure factor S_{hkl} and scattering amplitude $F(\vec{Q})$. As the atoms are displaced within the unit cell, the structure factor and intensity of the peak change.

8 Results of the UXRD Measurements

The time-resolved measurements are performed on all samples utilizing an 800 nm fs laser as pump pulse and X-ray pulses for probing. As the short-time dynamics of the samples are of great interest, the first 200 ps were recorded with a time-resolution of 1 ps and the late-time dynamics after 200 ps with a resolution of 200 ps. For establishing a reference for later discussion, the gold thin film's transient strain was investigated first. Following that, the AuNCs and AuLNCs are investigated for three excitation fluences each, at approximately 5.9, 10.7 and 14.7 mJ/cm^2. Since the fluence can only be determined with a 10 % uncertainty, both nanostructured samples can be assumed to be investigated for similar excitation conditions and thus, can be directly compared. After discussion of the overall appearances, the samples are compared in terms of the induced temperature change from the equilibrium to the quasi-static state. An explanation of the used evaluation tools and associated uncertainties is given in the following chapter.

Fast Fourier Transform

For quantitatively analyzing the oscillation frequencies and periods present in the measured transient strain signals, a Fast Fourier Transform (FFT) is performed. FFT is an algorithm for efficiently calculating a Discrete Fourier Transformation (DFT) with less computational effort by breaking the transformation down into multiple smaller transformations [49, 50]. The DFT transforms a discrete strain signal in a chosen time interval into the frequency domain and translates it into a sum of harmonic oscillations of different frequencies. The DFT is defined by:

$$S_k = \sum_{n=0}^{N-1} \eta_n e^{-2\pi i k n/N}. \tag{24}$$

Here, S_k denotes the complex Fourier coefficients that encode the amplitude and phase of the frequency components, the parameter N denotes the number of measurement points and η_n the individual strain-values for each discrete time-step.

Before transforming the raw strain data, constant background or offset of the signal is subtracted as it yields no information about the oscillations. The amplitude of the respective frequency component was calculated from the magnitude of the complex Fourier coefficients:

$$|S_k| = \sqrt{\mathrm{Re}(S)^2 + \mathrm{Im}(S)^2}. \tag{25}$$

Since the strain signal is strictly in the real dimension, only positive frequencies were considered in the analysis. The dominating frequency modes are identified via the maxima of the Fourier spectrum and the corresponding oscillation periods T were calculated by:

$$T = \frac{1}{f}. \tag{26}$$

Each FFT is performed only considering the response of the sample in first 200 ps after excitation. For later times, the oscillations cease and reach a quasi-static state. However, from the chosen limited time-interval $T_{\mathrm{meas}} = 200$ ps uncertainties for determining the frequency, and thus, the oscillation period arise. The frequency resolution is given by:

$$\Delta f = \frac{1000}{T_{\mathrm{meas}}} = 5\ \mathrm{GHz}. \tag{27}$$

The factor 1000 arises from unit conversion. Assuming

$$\sigma_f = \frac{\Delta f}{2}, \tag{28}$$

the frequency uncertainty σ_f amounts to 2.5 GHz and consequently, the oscillation period uncertainty is determined via

$$\sigma_T = \left(\frac{dT}{df}\right)\sigma_f = \frac{1000}{f^2}\sigma_f \tag{29}$$

for each frequency.

8.1 Gold Thin Film

The transient strain response of the 100 nm gold film, measured via the relative shift of the Au (111) broad and narrow peak, can be seen in fig. 17a) for a pump-fluence of 17.8 mJ/cm^2. For better readability, the moving average (continuous lines) taken over 10 adjacent strain data points is plotted as an overlay on the individual measured points (dots). Both peak contributions exhibit a similar overall appearance, however, at different amplitudes. The broad-peak transient exhibits a strain amplitude that is 2.5 times larger than the narrow peak, which originates from different RSS-factors. Since only the out-of-plane strain is considered, one can conclude that the crystallites or regions of differing crystallinity, from which the individual peak-contributions originate, are only in-plane. Thus, since the out-of-plane crystalline morphology is isotropic, only one of the transients has to be considered in a qualitative discussion.

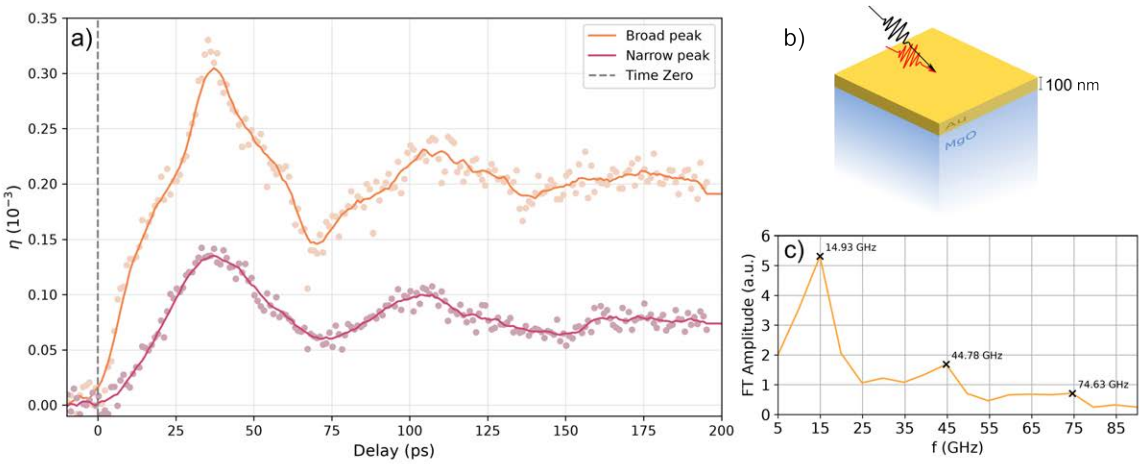

Figure 17: a) Transient strain of the thin film's broad (yellow) and narrow (purple) Au (111) reflection. For better readability, the moving average (continuous lines) taken over 10 adjacent strain data points is plotted as an overlay on the individual measurement points (dots). Both reflections exhibit similar dynamics: Immediately following excitation, the strain increases and subsequently displays a dampened oscillation around a quasi-static strain level. **b)** Schematic depiction of the gold thin film sample and pump and probe pulse. **c)** FFT of the broad Au (111) peak, exhibiting the three dominating oscillation frequencies.

The strain-values recorded at negative delays correspond to the time frame before the sample's excitation during which it remains in thermal equilibrium. Immediately following the excitation, an increase of the strain can be observed, indicating a rapid out-of-plane expansion of the gold film. The expansion reaches its maximum amplitude of 0.32‰ about 35 ps after excitation and subsequently displays a damped oscillation around a constant level of strain with magnitude 0.02‰. The timing of the first maximum is defined by the film thickness d and sound velocity $v_s = \sqrt{c_{3333}/\rho} = 3.45$ nm/ps [51] of the launched strain pulse: 35 ps $= d/v_s$. This corresponds to the time required for the strain pulse to propagate from the surface through the 100 nm layer to the substrate. The subsequent oscillation of the signal corresponds to the strain wave propagating through the film and being partially reflected at the surface and interface to

the MgO substrate, due to an acoustic-impedance mismatch between the gold film and the air surrounding it. As a portion of the strain pulse is transmitted into the substrate after every round trip through the gold layer, it loses amplitude and results in the strain transient's oscillation decaying over time. After three oscillations or round trips of the strain pulse in 200 ps the strain amplitude has almost decayed to the quasi-static strain-level of 0.2 ‰. The triangular-like shape of the maxima originates from the sharp interface of the surface, which results in sharp strain wave fronts. For a homogeneous excitation profile, the maxima are expected to be triangle-shaped. However, here, the first recorded maximum of the broad peak exhibits a plateau at approximately 20 ps, indicating the presence of an inhomogeneous component in the excitation profile, which influences the shape of the propagating strain wave [52]. For reference, the sketched strain wave shown in fig. 11 originates from an inhomogeneous excitation profile, which gives rise to its curved wave-front.

To quantitatively analyze the oscillation periods present in the strain signal, a FFT was performed, the results of which can be seen in fig. 17c). Prior to the transform, constant background was subtracted from the original strain signal. The background level was determined as the mean value of the entire strain signal over the 200 ps measurement interval, which in this case corresponds to the quasi-static strain level of 0.2 ‰. The three dominating frequencies identified in the Fourier spectrum and their corresponding oscillation periods are summarized in the following table 1:

Frequency [GHz]	Oscillation period [ps]
14.9 ± 2.5	67.0 ± 11.2
44.8 ± 2.5	22.4 ± 1.3
74.6 ± 2.5	13.4 ± 0.5

Table 1: Oscillation frequencies and periods of the gold thin film's strain transient

The 15 GHz peak corresponds to the (67.0 ± 11.2) ps oscillation period, given by the time difference between the most prominent maxima, observed at delays 35 ps, 102 ps and 169 ps. The higher frequency components at 44.8 GHz and 74.6 Ghz correspond to the third and fifth odd harmonics of the fundamental 15 GHz frequency. Their presence is characteristic of a triangular wave form observed in fig. 17.

The observed dampened oscillation of the transient strain and the triangular appearance of the maxima are in line with the expected response of a thin film to femtosecond laser excitation.

8.2 Gold Nanocubes

Following the characterization of the thin film reference sample, the nanostructured samples are investigated in a similar fashion. However, for an analysis of the heat transport to the substrate, the transient strain evolutions are measured over a much longer time frame and for three different pump pulse fluences to investigate the fluence-dependence of the response. In fig. 18a) the transient strain, measured via the Au (002) reflection is presented for excitation with 5.9 mJ/cm^2, 10.7 mJ/cm^2, and 14.8 mJ/cm^2 pump-fluences. All three transients exhibit a qualitatively similar appearance. Directly following the excitation, a comparatively large expansion is recorded, reaching maximum values of 0.55 ‰, 1.1 ‰ and 1.8 ‰ at approximately 45 ps, respectively. Subsequently, the expansion relaxes to an approximate third of the maximum strain until 65 ps before rising slowly again to the initial maximum expansion over 112 ps. After reaching the second maximum at approximately 177 ps, the strain slowly decays over 6 ns.

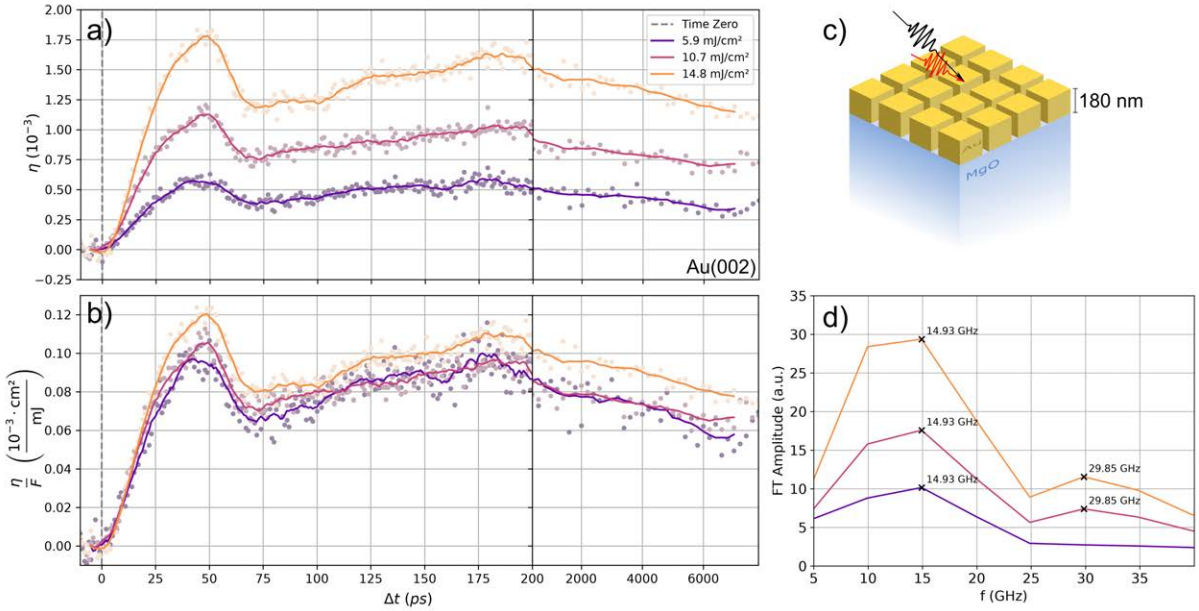

Figure 18: a) Strain transient of the AuNCs Au (002) reflection for different pump fluences. All transients exhibit a similar behavior of an immediate increase after excitation and subsequent slight decrease until approximately 65 ps. The strain amplitude increases slowly again until 177 ps and finally decreases over 6 ns. **b)** All strain transients from a) normalized over their respective excitation fluence to demonstrate the near-linear relationship between strain and fluence. The transient measured at 14.8 mJ/cm^2 exhibits a slight non-linearity. **c)** Schematic depiction of the AuNCs. **d)** FFT of the transients depicted in a) exhibit their two dominating frequencies.

It is important to note that during the course of the measurement, the spot size of the pump pulse on the sample surface has changed due to astigmatism in the pump beam. This leads to an overestimation of the final relaxation and underestimation of the quasi-static strain level, which is corrected by a scaling factor $A(t_0)/A(t)$. Since the strain change linearly depends on the pump fluence change, the strain transient is corrected by multiplying it with a time-dependent factor that takes this changing spot size into account:

$$\eta_{\text{corrected}} = \eta_0 \cdot \frac{A(t_0)}{A(t)} \tag{30}$$

where η_0 is the raw strain data, t the delay, t_0 the starting time, $A(t_0)$ the pump-spot size measured at the beginning of the measurement and $A(t)$ the spot size measured at the end of the measurement, assuming that its size increases linearly over time. For larger delays, the scaling factor is largest (≈ 1.5), for smaller ones, it approaches 1. Now the slow strain relaxation is more accurate to the real relaxation rate. Still, the corrected strain amplitude relaxes about 35 % from the second strain maximum.

A notable feature of the transients is the asymmetry of the first maximum, which exhibits a longer rise time than relaxation time. This might be a result of the interaction of multiple strain pulses launched from different sides of the AuNCs, as absorption is not limited to the top of the cubes.

The FFT, depicted in fig. 18d), reveals the same dominating oscillation frequencies of (14.93 $\pm$ 2.5) GHz and (29.85$\pm$ 2.5) GHz for the two highest fluences and one (14.93 $\pm$ 2.5) GHz frequency for the lowest fluence of 5.9 mJ/cm^2.

The frequency of (14.9 $\pm$ 2.5) GHz corresponds to an oscillation period of about (67.0 $\pm$ 11.2) ps, which, most likely, corresponds to the strain pulse propagating from the surface to the backside of the 180 nm cubes. Since the nanoparticles' dimension is twice as thick as the thin film's, it is surprising to see a similar oscillation period.

The second observed frequency of (29.9 ± 2.5) GHz corresponds to the second harmonic of the fundamental 14.9 GHz frequency. In contrast to the thin film, where odd harmonics where present, the presence of an even harmonic indicates a more complex strain pulse shape.

To investigate the assumption that the strain scales linearly with the incident fluence, the three strain curves were normalized over their respective incident fluence, shown in fig. 18b). While the transients measured at 5.9 mJ/cm^2 and 10.7 mJ/cm^2 overlap nicely after normalization, verifying the assumed linear scaling of the strain amplitude with the fluence, the transient normalized over 14.8 mJ/cm^2 exhibits a slight offset and lies above the lower-fluence curves. This suggests a non-linear response as the strain increases at a faster scale at higher excitation fluences.

8.3 Gold L-Chiral Nanocubes

The fluence-dependent strain evolution for the l-chiral AuNCs can be seen in fig. 19, with panels a) and b) showing the transients for the Au (002) and Au (111) reflections, respectively. Both reflections exhibit a qualitatively similar behavior. Immediately after excitation, both peaks show a large expansion that reaches its maximum at approximately 37 ps. While the strain of the Au (002) peak, measured at 5.8 mJ/cm^2, 10.9 mJ/cm^2 and 15.2 mJ/cm^2 reaches its maximum at approximate strain values of 1.25 ‰, 2.0 ‰ and 2.8 ‰, respectively, the Au (111) transients show a slightly larger out-of-plane expansion, reaching maximum values of 1.5 ‰, 2.4 ‰ and 3.1 ‰, respectively. The overall appearance of the transient resembles that of the AuNCs; a first large maximum, followed by a small and slow relaxation over 63 ps and a subsequent slow expansion to nearly the first strain-maximum's level. However, the LAuNCs show an overall larger strain for all excitation fluences. Moreover, the LAuNC transients are modulated by higher-frequency oscillations. For the Au (111) reflection, some of these higher frequencies can be attributed to a higher noise level, nevertheless, they can be clearly seen modulating the Au (002) transient. From the static RSM (see fig. 9), it was concluded, that the smaller intensity of the Au (111) peak in the RSM originates from a smaller amount of crystallites being oriented in this direction or part of the cubes being tilted relative to the sample surface[2]. Reasonably, the Au (111) peak exhibits a higher signal-to-noise ratio as fewer crystallites contribute to the diffraction process.

Moreover, a plateau in the first maximum of the transients, similar to the one observed for the thin film, is present. However, its presence here is most likely due to a more complex reason other than inhomogeneous excitation conditions, as the LAuNCs have a much more complex morphology, for which multiple factors have to be considered. The FFTs of the transients, shown in fig. 19e), f) for the Au (002) and Au (111) reflections, respectively, reveal a number of dominating frequencies, that are summarized in table 2 below:

Frequency [GHz]	Oscillation period [ps]
9.9 ± 2.5	100.5 ± 25.3
44.8 ± 2.5	22.4 ± 1.3
54.7 ± 2.5	18.3 ± 0.8
94.5 ± 2.5	10.6 ± 0.3

Table 2: Oscillation frequencies and periods of the LAuNCs' strain transient

Both reflections exhibit a frequency of (9.9 ± 2.5) GHz for all considered excitation fluences, corresponding to an oscillation period of (100.5 ± 25.3) ps. The oscillations of higher frequency that modulate the

[2]The sample surface for the nanostructured samples, meaning the AuNCs and LAuNCs, is defined by their preferred orientation, lying flat on one side. Because not all of the individual cubes follow this orientation, their positioning is described as being tilted to this average surface plane.

transients measured for excitation 5.8 mJ/cm^2 and 10.9 mJ/cm^2 correspond to a (22.4 ± 1.3) ps period. Notably, the (44.8 ± 2.5) GHz frequency is not a harmonic of the fundamental (9.9 ± 2.5) GHz frequency, indicating, that it originates from the complex chiral morpholgy of the helicoids.

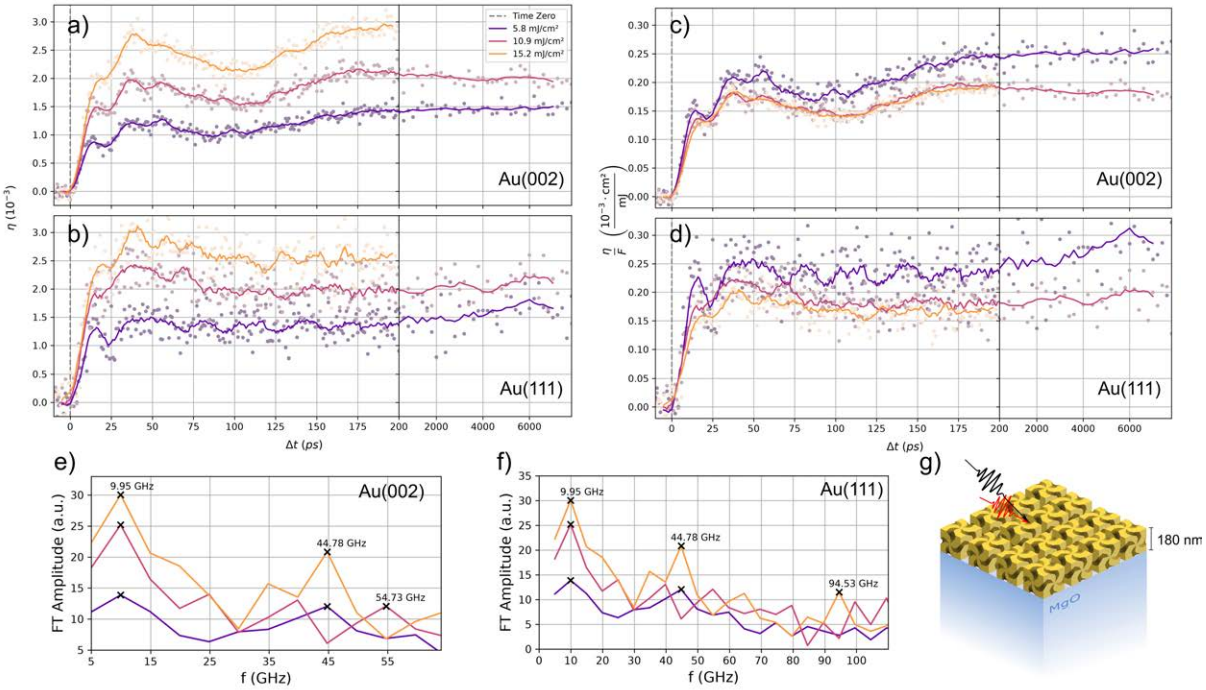

Figure 19: a) Transient strain of the LAuNCs' Au (002) reflection for three excitation fluences. Apart from the higher amplitude, the transients exhibit similar dynamics to the AuNCs. After excitation at 0 ps, the strain amplitude increases until approximately 37 ps, decays slightly until 100 ps and increases again to about the first maximum's level until 200 ps. The transients are additionally modulated by smaller and faster oscillations. **b)** Transient strain of the LAuNCs' Au (111) reflection for three excitation fluences. **c)**, **d)** The strain transients from a) and b), respectively, normalized over their excitation fluences. **e)**, **f)** FFTs of the transients depicted in a) and b), respectively. Both exhibit (9.9 ± 2.5) GHz and (44.8 ± 2.5) GHz oscillation frequencies. **g)** Schematic depiction of the LAuNCs.

To investigate the relationship between the strain amplitude and fluence, all transients were normalized by their respective fluence, the result of which can be seen in fig. 19c), d).

Interestingly, linear and non-linear scaling can be found again. However, the non-linear scaling of the strain now manifests for the lowest excitation fluence of 5.9 mJ/cm^2, in contrast to the AuNCs where the non-linearity appeared at the highest fluence. While this could be a result of bad overlapping of the pump and probe pulse, and therefore, incorrect determination of the pump fluence, it could also suggest that the strain response of the AuNCs and LAuNCs is much more complex than that of the thin films and many influencing factors, such as the more intricate morphology and absorption dynamics, have to be considered.

9 Discussion of the Time-Resolved Results

In this chapter, the experimental findings from the previous chapter are compared and interpreted. The transient strain curves of the three samples of interest, the gold thin film, the AuNCs, and the LAuNCs are compared in the context of their overall appearance, specific features, and strain amplitudes. The focus lies on the early-time dynamics, during the first 200 ps, as here, the transients exhibit the most differences, and because in this time frame the lattice dynamics do not solely originate from heat diffusion but also from strain pulse dynamics.

After extracting the exact differences, possible explanations are systematically explored by comparing the temperature increase calculated from the measured quasi-static strain amplitude to the expected one that can be calculated by considering the absorbed energy and specific heat capacity of the samples. In addition, the expected behaviors of homogeneous thin films and nanostructured films and their implications for the expected temperature and strain increase are discussed.

A comparison has to be made under careful consideration of the different systems and reveals deviations from the expected dynamics.

Firstly, the samples differ in thickness. While the gold thin film is approximately 100 nm thick (out-of-plane), the nanostructured AuNCs and LAuNCs are almost twice as thick at 180 nm. Assuming that all samples are investigated under the same excitation conditions and absorb the same amount of the pump fluence, a sample of larger volume distributes the same energy throughout a larger system, and thus, heats up less compared to a smaller film. Since the strain linearly scales with the temperature, a thinner film is expected to exhibit a larger strain amplitude.

However, the oscillation amplitudes, observed for the chiral and simpler nanoparticles, are approximately 5 to 10 times larger, respectively, even though the pump fluence, with which the thin film was excited, is about 1.6 times larger. Additionally, since the nanoparticles are almost twice as thick as the thin film, it is at first sight surprising to observe a similar oscillation period. This may be attributed to their more complex geometry, which can alter the strain response. While these similar oscillation periods are noted here, the subsequent analysis will focus on the amplitude differences.

Secondly, the morphological constraints of the samples differ. A thin film is expected to respond differently to laser excitation because the in-plane expansion of the lattice is suppressed, and therefore, the contractive stress due to the Poisson effect is missing. This leads to a larger out-of-plane strain. On the other hand, free-standing nanoparticles that are not coupled to a substrate can expand isotropically, in-plane and out-of-plane. Thus, for the same absorbed fluence, a thin film is expected to exhibit a larger out-of-plane expansion than a nanostructured film of the same dimensions, in which the expansion is distributed across all spatial directions. The schematic in fig. 20 compares the expected morphology-dependent expansion or strain. A continuous and substrate-bound thin film, subject to the Poisson effect, typically exhibits a larger out-of-plane expansion while a nanostructured and free-standing film can expand in both the in-plane and out-of-plane direction, effectively reducing the out-of-plane contribution. [11, 53]

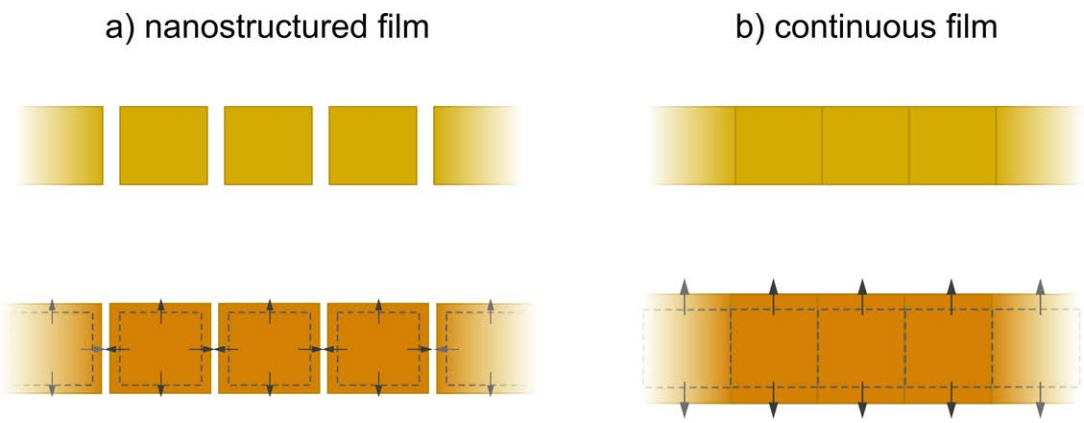

Figure 20: Schematic depiction of the morphology- and boundary-dependent strain. A free-standing nanostructured film **a)** can expand isotropically, which leads to a comparatively smaller out-of-plane expansion. A continuous and free-standing thin film **b)** experiences suppression of in-plane expansion and can therefore only expand out-of-plane. The schematic is adapted from [11].

Keeping these relations between strain, sample thickness and morphology in mind, the recorded experimental data is interpreted. To ensure the validity of a comparison, the transients are normalized with respect to their excitation fluence and film thickness. This must be done because the observed strain depends not only on the excitation fluence, as previously proven by the recorded fluence series for the AuNCs and LAuNCs, but also on the sample thickness.

9.1 Comparison of the Results

In fig. 21 the transient strain evolutions of the gold thin film, AuNCs, and LAuNCs, normalized to their respective fluence and film thickness are presented. For the gold thin film the broad-peak transient, measured at 17.8 mJ/cm^2 is chosen, for the AuNCs and LAuNCs the transients measured at 10.7 mJ/cm^2 and 10.9 mJ/cm^2 are chosen, respectively.

From previous analysis of the normalized fluence series for the AuNCs, it was concluded that the highest excitation fluence of 14.8 mJ/cm^2 exhibits some non-linearity. Similarly, the lowest excitation fluence of 5.8 mJ/cm^2 for the LAuNCs exhibits non-linear behavior as well. Thus, to allow for a more accurate comparison, free from non-linear effects, the second-highest excitation fluences were chosen. In the plot, the smoothed transients without the individual data points are exhibited so that the dynamics can be compared more easily.

From fig. 21, which compares the transients, the difference in strain amplitude is immediately obvious. The LAuNCs possess a normalized quasi-static amplitude that is approximately 2.1 times larger than that of the AuNCs and 31 times larger than that of the thin film. The normalized quasi-static amplitude of the AuNCs is approximately 15 times larger than that of the thin film. Next to the differences in amplitude, the strain dynamics or the shape of the transients differ. While the thin film exhibits a comparatively small expansion, reaching its first maximum at 35 ps, the AuNCs exhibit a much larger expansion with its maximum at 65 ps and the LAuNCs an even larger expansion with its dominant maximum around the same time as the thin film, at 37 ps, though an exact timing is difficult to determine due to the modulation by smaller oscillations.

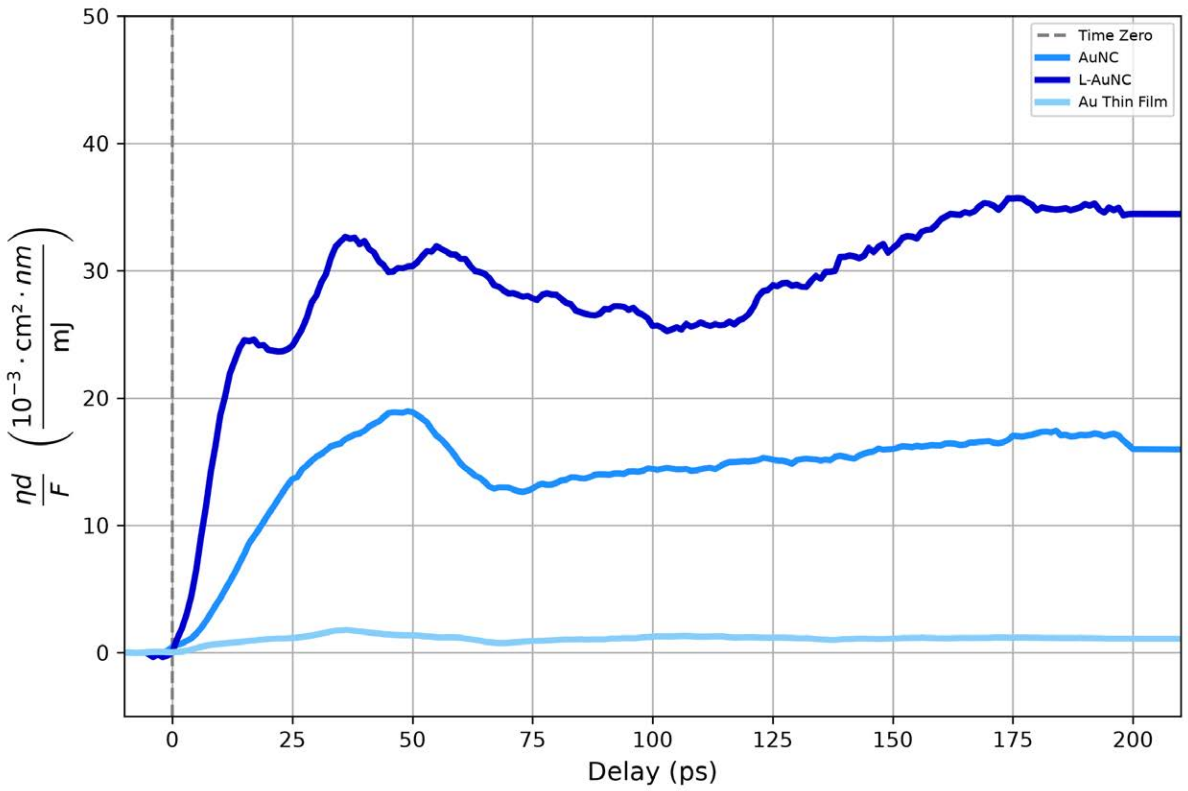

Figure 21: Comparison of the gold thin film and nanostructured sample strain transients, each normalized over their respective fluence and film thickness to allow for a more direct comparison.

While the AuNCs exhibit one larger maximum and a smaller one much later at 177 ps, the LAuNCs' second maximum is at a higher amplitude and much more distinct. The thin film's transient, however, exhibits a lot less apparent oscillations due to the scaling in the plot and appears almost constant in comparison. Furthermore, the main difference between the LAuNCs' and AuNCs' transients next to the difference in amplitude is the LAuNCs' modulation by smaller oscillations.

A comparison of the FFT spectra reveals a possible origin. While the thin film only exhibits odd harmonics at (14.9 ± 2.5) GHz, (44.8 ± 2.5) GHz, and (74.6 ± 2.5) GHz, consistent with a triangular strain pulse shape, the AuNCs exhibit a fundamental mode at (14.9 ± 2.5) GHz and a second harmonic at (29.9 ± 2.5) GHz, indicating a more complex strain pulse shape. In contrast, the LAuNCs exhibit two frequencies, at (9.9 ± 2.5) GHz and (44.8 ± 2.5) GHz, which are not harmonically related. This observation suggests that the LAuNCs' modulation originates from the complex chiral nanostructuring.

The differences in the overall shape or dynamics can be partially explained by qualitative analysis. The AuNCs' and LAuNCs' transients exhibit some resemblance, since both show two larger oscillations during the 200 ps measurement interval. A possible explanation for the fast modulation of the LAuNCs' strain is presented by the smaller chiral arms on top of the cubes having more degrees of freedom and oscillating faster compared to the inner structure. The FFT of the LAuNCs' transient revealed oscillation periods of (18.27 ± 0.83) ps that could likely originate from these structures. For visualizing this, these smaller oscillations were extracted from the transient by subtracting the larger background oscillation. The result is depicted in fig. 22. The FFT of these oscillations reveals a period of (21.56 ± 1.16) ps, and therefore, verifies that the ≈ 20 ps oscillation does indeed originate from the chiral arms.

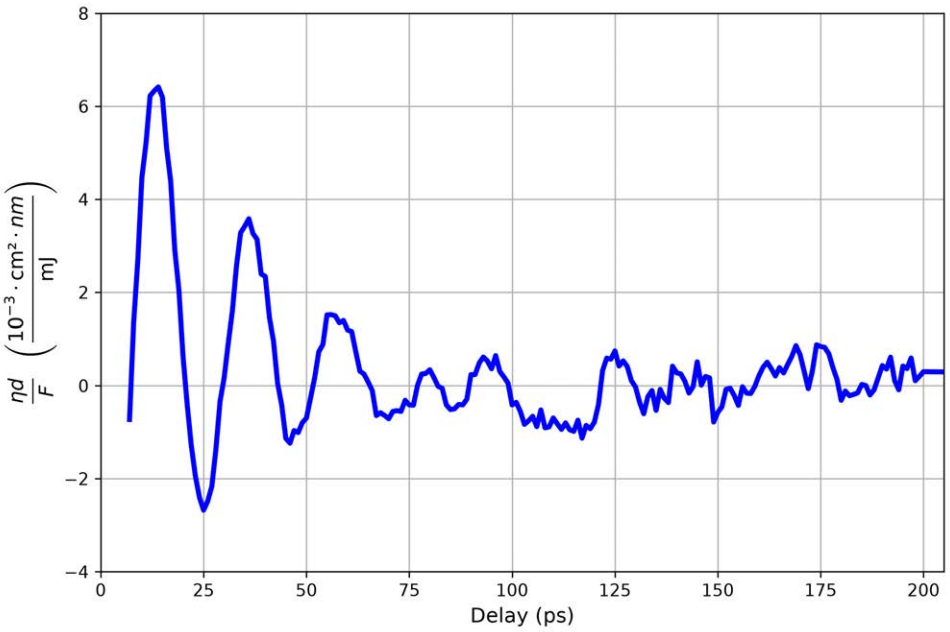

Figure 22: Visualization of the oscillations. A FFT of the oscillations reveals a (46.39 ± 2.5) GHz frequency and (21.56 ± 1.16) ps oscillation period.

Additionally, since these oscillatory features are absent in the AuNCs, they could be related to chirality-driven phonon dynamics. In 2023, *K. Ishito et al.* experimentally observed chiral phonons in a three-dimensional bulk α-HgS crystal with circularly polarized Raman scattering [3]. Therefore, chiral crystals can, in principle, host chiral phonons and this could potentially explain the observed strain dynamics in the LAuNCs. However, definitive identification of such chiral phonons requires further research.

For the interpretation of the different strain amplitudes, it is resonable to analyze the temperature increase of the individual samples, since temperature is an ensemble-averaged, intensive quantity that probes the lattice or phonon temperature, and thus, the lattice displacement that governs thermal expansion. This approach allows for investigation of the lattice expansion's origin, i.e., if the observed strain at quasi-static timescales purely originates from the absorbed pump fluence. Specifically, if the strain indeed originates purely from the absorbed pump fluence, the temperature increase determined from the quasi-static strain via the heat expansion coefficient must be equivalent to the temperature increase expected from the absorbed energy density and heat capacity. Thus, the analysis will commence with calculation and comparison of these temperature changes, and any deviations from this equality have to be investigated thereafter. Possible reasons for deviations for the samples can include size-dependent thermodynamic effects and differing absorption mechanisms, which will be discussed in more detail later this chapter.

9.2 Temperature Change Determined from the Quasi-Static Strain

A valid approach to determine the temperature increase is via the quasi-static strain, at time scales where the electronic and phononic system have equilibrated [54]. The values obtained from the Bragg-peak shift in the reciprocal space provide an accurate measure of the sample's temperature and will therefore serve as the benchmark for analyzing the origin of the observed temperature rise.

The quasi-static strain amplitudes are determined from the transients shown in fig. 17, fig. 18, and fig. 19 at 200 ps and are summarized in table 3:

The nanostructured samples can be assumed to have been measured under identical excitation conditions given that the fluence can only be determined with a 10 % uncertainty. Nonetheless, the thin film's strain

Sample	η_{qs} [10^{-3}]	Pump fluence [mJ/cm^2]
Gold thin film	0.2	17.8
AuNC	1.0	10.9
LAuNC	2.1	10.7

Table 3: Quasi-static strain amplitudes

amplitude must be scaled to a similar fluence to ensure comparability. Assuming a linear dependence of the strain amplitude on the pump fluence, the thin film's quasi-static strain amplitude at $10.7 \cdot 10^{-3}$ can be estimated as:

$$\eta_{\mathrm{qs}}^{\mathrm{TF}}(F = 10.7\ \mathrm{mJ/cm^2}) = \eta_{\mathrm{qs}}^{\mathrm{TF}}(F = 17.8\ \mathrm{mJ/cm^2}) \cdot \frac{10.7}{17.8} = 1.2 \cdot 10^{-4} \tag{31}$$

The corresponding temperature rise is now derived from the determined quasi-static out-of-plane strain amplitudes η_{qs} and the thermal expansion coefficient α [11]:

$$\Delta T_\eta = \frac{\eta_{\mathrm{qs}}}{\alpha}. \tag{32}$$

It should be noted that the thermal expansion coefficient is in fact temperature-dependent but can be approximated as being constant for small ΔT above 200 K [55]. Since the upper limit of the expected temperature increase is approximately 150 K, a constant value of $\alpha = 14.2 \cdot 10^{-6}$ 1/K is used. Moreover, utilizing a linear thermal expansion coefficient assumes an isotropic morphology. Thus, the following temperatures are calculated for each of the three samples, assuming they are excited with a fluence of about 10.7 mJ/cm^2:

$$\Delta T_\eta^{\mathrm{TF}} = 8.45\ \mathrm{K}, \tag{33}$$

$$\Delta T_\eta^{\mathrm{AuNC}} = 70.42\ \mathrm{K}, \tag{34}$$

$$\Delta T_\eta^{\mathrm{LAuNC}} = 147.89\ \mathrm{K}. \tag{35}$$

While the values obtained for the free-standing nanostructured samples are accurate, the in-plane boundary conditions differ for the thin film, since the Poisson stress enhances the out-of-plane expansion. Consequently, employing the near-equilibrium linear thermal expansion coefficient is inadequate in this case and leads to an overestimation of the temperature rise. Instead, a modified expansion coefficient that accounts for this Poisson contribution must be derived [11, 47].

9.2.1 Deriving the Ultrafast Thermal Expansion Coefficient

In the following, the arguments, that lead to the concept of an "ultrafast expansion coefficent", which is a consequence of the Poisson effect, are summarized. A detailed explanation is given by *M. Mattern et al.* [11], which will be summarized here. Generally, the strain response to a time- and space-dependent stress is a solution of the 3D elastic wave equation:

$$\rho_m \frac{\partial^2 u_i}{\partial t^2} = \sum_j \frac{\partial}{\partial x_j} \sigma_{ij}^{\text{tot}} \tag{36}$$

where ρ_m denotes the mass density, σ_{ij}^{tot} the total stress driving the atomic motion, and u_i the atom's displacement. The total stress is composed of an elastic stress contribution in response to an existing strain and an external, laser-induced contribution:

$$\sigma_{ij}^{\text{tot}} = \sigma_{ij}^{\text{elastic}} - \sigma_{ij}^{\text{ext}}, \qquad \text{with} \quad \sigma_{ij}^{\text{elastic}} = \sum_{k=1}^{3} \sum_{l=1}^{3} c_{ijkl}\, \eta_{kl}. \tag{37}$$

The elastic stress is linked to the strain tensor η_{kl} via Hooke's law where c_{ijkl} are the direction-dependent elastic constants. Inserting eq. (37) into eq. (36) yields:

$$\rho_m \frac{\partial^2 u_i}{\partial t^2} = \sum_j \frac{\partial}{\partial x_j} \left(\sum_{k,l} c_{ijkl}\, \eta_{kl} \; - \sigma_{ij}^{\text{ext}} \right). \tag{38}$$

Focusing on the out-of-plane direction (i=3) of interest, the elastic wave equation becomes:

$$\begin{aligned} \rho_m \frac{\partial^2 u_3}{\partial t^2} &= \frac{\partial \sigma_{13}^{\text{tot}}}{\partial x_1} + \frac{\partial \sigma_{23}^{\text{tot}}}{\partial x_2} + \frac{\partial \sigma_{33}^{\text{tot}}}{\partial x_3} \\ &= \frac{\partial (\sigma_{13}^{\text{elastic}} - \sigma_{13}^{\text{ext}})}{\partial x_1} + \frac{\partial (\sigma_{23}^{\text{elastic}} - \sigma_{23}^{\text{ext}})}{\partial x_2} + \frac{\partial (\sigma_{33}^{\text{elastic}} - \sigma_{33}^{\text{ext}})}{\partial x_3}. \end{aligned} \tag{39}$$

Eq. (39) simplifies further by neglecting the shear forces and focusing on the laser-induced stresses σ_{ii}^{ext} and strains η_{kk}:

$$\rho_m \frac{\partial^2 u_3}{\partial t^2} = \frac{\partial (\sigma_{33}^{\text{elastic}} - \sigma_{33}^{\text{ext}})}{\partial x_3}. \tag{40}$$

In the same way, the elastic stress $\sigma_{33}^{\text{elastic}}$ is simplified, so that only the diagonal entries remain, assuming an isotropic, cubic crystal lattice:

$$\sigma_{33}^{\text{elastic}} = c_{3333}\, \eta_{33} + \sum_{k \neq 3} c_{33kk}\, \eta_{kk}, \text{ for } k = 1, 2. \tag{41}$$

Thus, the elastic wave equation, reduced to the longitudinal stress contribution becomes:

$$\begin{aligned} \rho_m \frac{\partial^2 u_3}{\partial t^2} &= \frac{\partial}{\partial x_3} (c_{3311}\, \eta_{11} + c_{3322}\, \eta_{22} + c_{3333}\, \eta_{33} - \sigma_{33}^{\text{ext}}) \\ &= \frac{\partial}{\partial x_3} (\sigma_{33}^{\text{elastic}} + \sigma_{33}^{\text{Poi}} - \sigma_{33}^{\text{ext}}), \end{aligned} \tag{42}$$

which can be further reduced by assuming laterally homogeneous excitation of the probed sample region. For experiments on thin films, this is valid because the pump spot's footprint (sub µm) is much smaller than the film thickness (few hundred nm) and the probe pulses' footprint. Hence:

$$\rho_m \frac{\partial^2 u_3}{\partial t^2} = \frac{\partial}{\partial x_3} (c_{3333}\, \eta_{33} - \sigma_{33}^{\text{ext}}). \tag{43}$$

In the quasi-static state the total stress vanishes due to the elastic and Poisson stress contribution compensating it. The time derivative vanishes and the elastic wave equation becomes:

$$\eta_{33}^{\mathrm{qs}} = \frac{\sigma_{33}^{\mathrm{ext}}}{c_{3333}} - \sum_{k\neq 3} \frac{c_{33kk}}{c_{3333}}\, \eta_{kk}^{\mathrm{qs}} \tag{44}$$

where the last term describes the Poisson stress. Up until now, only films that can expand isotropically were considered ($\eta_{11}^{\mathrm{qs}} = \eta_{22}^{\mathrm{qs}} = \alpha\ \Delta T_\eta$):

$$\sigma_{33}^{\mathrm{ext}} = (c_{3333} + 2c_{3311})\ \alpha \Delta T_\eta \tag{45}$$

and

$$\eta_{33}^{\mathrm{qs}} = \alpha \Delta T_\eta. \tag{46}$$

However, for substrate-bound thin films, the in-plane strain contributions vanish ($\eta_{11}^{\mathrm{qs}} = \eta_{22}^{\mathrm{qs}} = 0$), and therefore:

$$\eta_{33}^{\mathrm{qs}} = \frac{\sigma_{33}^{\mathrm{ext}}}{c_{3333}} - 0. \tag{47}$$

The laser-induced stress $\sigma_{33}^{\mathrm{ext}}$ is related to the deposited energy density ρ_Q via the Grüneisen parameter:

$$\sigma_{33}^{\mathrm{ext}} = \Gamma_3\ \rho_Q \tag{48}$$

with

$$\rho_Q = C_V \cdot \Delta T_\eta. \tag{49}$$

Eq. (47) then becomes:

$$\eta_{33}^{\mathrm{qs}} = \frac{\Gamma_3\ \rho_Q}{c_{3333}} = \alpha^{\mathrm{uf}} \Delta T_\eta. \tag{50}$$

To simplify the expression for the Grüneisen parameter, the ultrafast thermal expansion coefficient α_{uf} is introduced:

$$\Gamma_3 = \frac{c_{3333}}{C_V} \underbrace{\left(\alpha_3 + \sum_{k\neq 3} \frac{c_{33kk}}{c_{3333}} \alpha_k \right)}_{\alpha_{\mathrm{uf}}} \tag{51}$$

with

$$\alpha^{\mathrm{uf}} = \alpha_3 \left(1 + \sum_{k\neq 3} \frac{c_{33kk}\alpha_k}{c_{3333}\alpha_3} \right). \tag{52}$$

For isotropic materials like gold, the linear thermal expansion coefficient and the elastic constants simplify to: $\alpha_i = \alpha$ and $c_{3311} = c_{3322} = c_{12}$. Therefore:

$$\alpha^{\mathrm{uf}} = \alpha \left(1 + 2 \cdot \frac{c_{3311}}{c_{3333}} \right). \tag{53}$$

The Poisson ratio for metals is approximately $\nu = \frac{c_{3311}}{c_{3333}+c_{3311}} \approx 1/3$. Thus, the linear and ultrafast thermal expansion coefficients relate via:

$$\alpha^{\mathrm{uf}} \approx 2\alpha. \tag{54}$$

The temperature change with respect to the in-plane boundary conditions is now calculated via:

$$\Delta T_{\eta}(\alpha_{\mathrm{uf}}) = \frac{\eta_{\mathrm{qs}}}{\alpha_{\mathrm{uf}}} = \frac{\eta_{\mathrm{qs}}}{2\alpha}. \tag{55}$$

The assumption $\alpha_{\mathrm{uf}} \approx 2 \cdot \alpha$ is valid only for the quasi-static timescale. For later timescales, after few nanoseconds, the film relaxes laterally, and thus, a near-equilibrium linear thermal expansion is restored. The thin film's correct temperature rise with consideration of the Poisson effect is calculated as:

$$\Delta T_{\eta}^{\mathrm{TF}}(\alpha_{\mathrm{uf}}) = 4.23\ \mathrm{K}. \tag{56}$$

In summary, the thin film exhibits a temperature increase of 4.23 K, the AuNCs of 70.42 K and the LAuNCs of 147.89 K, for a pump fluence of about 10.7 mJ/cm^2. These values are now compared to the expected temperature changes originating from the absorbed pump fluence followed by a discussion of the underlying absorption mechanics.

9.2.2 Expected Laser-Induced Temperature Change

The expected laser-induced temperature change is estimated from the absorbed pump fluence via [12]:

$$\Delta T_F = Abs \cdot \frac{F}{C_V \cdot d}, \tag{57}$$

where F is the incident pump fluence, d the film thickness and C_V the heat capacity per constant volume. However, the incident fluence must be corrected for the absorbance Abs. Utilizing the complex refractive index $\tilde{n} = n + ik$ of gold at an incident wavelength of 800 nm with $n = 0.15$ and $k = 4.91$ [51,56] at an incidence angle of 51°, the absorbance is calculated via:

$$Abs \ = \ 1 - R_p \ = \ 1 - (r_p \cdot r_p^*) \tag{58}$$

where R_p is the reflectance and r_p the complex amplitude coefficients for reflection of p-polarized light, derived from the Fresnel equations [57]:

$$r_p = \frac{n_2 \cos\theta_i - n_1 \cos\theta_t}{n_2 \cos\theta_i + n_1 \cos\theta_t}. \tag{59}$$

This yields an absorbance of 3.72 %. The heat capacity C_V of gold is dominated by the phononic contribution and can be assumed as constant, as the measurements are conducted at room temperature (300 K), which is well above the Debye temperature of 190 K for gold [55]. Utilizing $C_V = 2.49 \cdot 10^6$ J/m^3 K [58,59], the laser-induced temperature change of the 100 nm thin film is estimated:

$$\Delta T_F^{\mathrm{TF}}(d) = 15.9\ \mathrm{K}. \tag{60}$$

For the nanostructured samples, such straight-forward calculation is not sufficient as directly inserting the 180 nm edge length into d leads to an underestimation of the temperature rise. Instead, an effective film thickness or equivalently, a correction factor for the film thickness must be derived for the AuNCs and LAuNCs, respectively.

Effective Film Thickness of AuNCs

For the AuNCs, the correction factor is given by the ratio of the area coverage of the cubes on the substrate to their surface area. The area coverage is determined from the cube's top surface area (180 nm · 180 nm) and the average distance (≈ 20 nm) between the cubes, estimated from the SEM image in fig. 2. Thus, each cube occupies an estimated effective area of 200 nm by 200 nm. Since the pump laser is incident at an angle of 51° and the penetration depth is insufficient to excite the substrate, direct absorption by the substrate in the gaps between the cubes can be neglected and consequently, the incident pump fluence can be considered to be absorbed exclusively within the effective area of the cubes. A schematic depiction of these estimates can be seen in fig. 23.

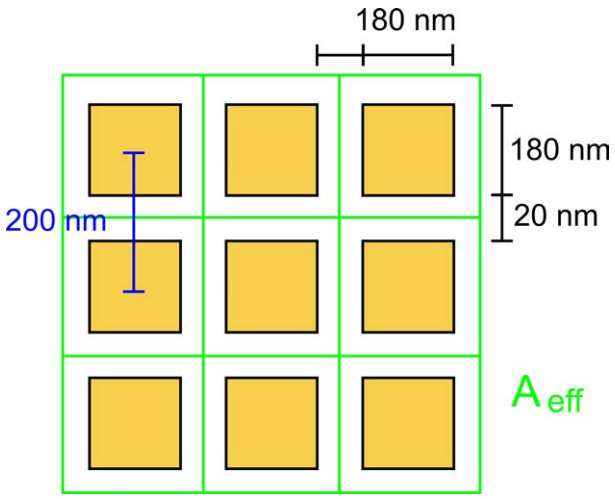

Figure 23: Schematic depiction of the AuNC's estimated distances and effective area.

The correction factor ζ_{AuNC} is therefore:

$$\zeta_{\text{AuNC}} = A_{\text{cov}} = \frac{(180\ \text{nm})^2}{(200\ \text{nm})^2} = 0.81 \tag{61}$$

and consequently, the laser-induced temperature rise:

$$\Delta T_F^{\text{AuNC}} = \text{Abs} \cdot \frac{\text{F}}{\text{C}_V \cdot \text{d} \cdot \zeta_{\text{AuNC}}} = 11.1\ \text{K}. \tag{62}$$

This approach is analogous to estimating the film thickness the nanocube sample would have if they were to be melted down into a homogeneous thin film and spread out over their original area.

Effective Film Thickness of LAuNCs

A similar approach is applied to estimate the LAuNCs' effective film thickness, although, their additional nanostructuring must be taken into account. A straight-forward, though rough estimation of their volume, is performed by dividing the LAuNCs into 3x3x3 grid of 27 individual smaller cubes with an edge length of 60 nm, a visualization of which is depicted in fig. 24a). The four "notches" on each side are subtracted and count as a missing smaller cube. The remaining volume of one individual LAuNC is proportional to 15 $(60\ \text{nm})^3$ cubes (see fig. 24b)) which is 55.5 % of the solid AuNCs' volume.

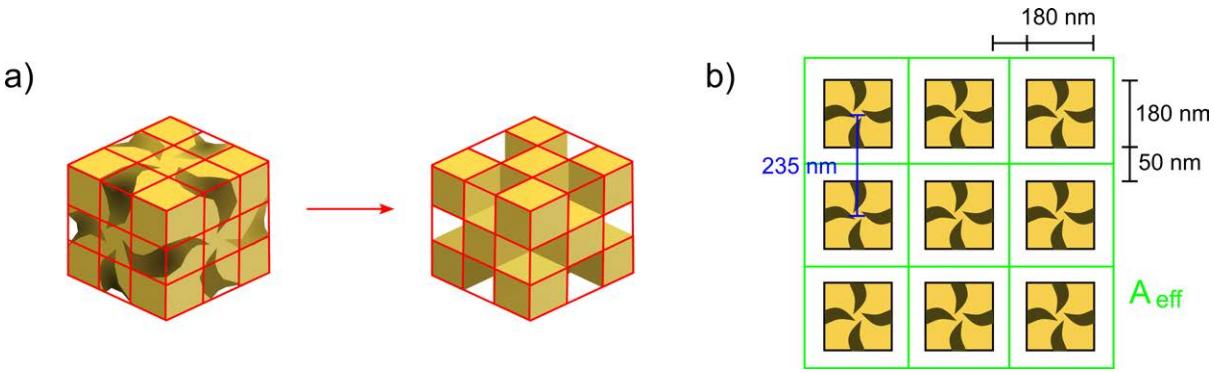

Figure 24: **a)** Estimation of the LAuNCs' volume by dividing them into 27 smaller cubes. The 4 "notches" on each side are subtracted, leaving 15 cubes. **b)** Schematic depiction of the LAuNCs' estimated distances and effective areas.

Again, the average distance between the cubes is estimated from the SEM image in fig. 2, to approximately 55 nm. The effective area per individual cube is 200 nm · 200 nm, yielding an areal coverage of:

$$A_{\text{cov}} = \frac{(180\text{ nm})^2}{(235\text{ nm})^2} = 0.59. \tag{63}$$

Combining this with the volume fraction yields the correction factor:

$$\zeta_{\text{LAuNC}} = \text{A}_{\text{cov}} \cdot 0.55 = 0.33. \tag{64}$$

Consequently, the laser-induced temperature rise of the LAuNCs is estimated as:

$$\Delta T_F^{\text{LAuNC}} = Abs \cdot \frac{F}{C_V \cdot d \cdot \zeta_{\text{LAuNC}}} = 26.98\text{ K}. \tag{65}$$

An overview of the temperature changes calculated via the different approaches is summarized in table 4 below. A comparison of the temperature rise determined from the quasi-static strain to the one expected from the absorbed laser fluence reveals some discrepancies. Nonetheless, the most apparent result is that the nanostructured samples experience a much larger temperature rise than the thin film. While the thin-film temperature, determined from the quasi-static strain, is relatively small at 4.2 K, the AuNCs experience a 16.8 times larger and the LAuNCs a 35.2 times larger temperature rise. These differences were also apparent in transients normalized over the film thickness and pump fluence, shown in fig. 21.

Sample	ΔT_η	ΔT_F	d_{eff}	Utilized heat expansion coefficient
Gold thin film	4.2 K	15.9 K	100 nm	α_{uf}
AuNC	70.4 K	11.1 K	145.8 nm	α
LAuNC	147.9 K	26.98 K	58.94 nm	α

Table 4: Comparison of measured temperature changes and ones expected without additional plasmonic absorption

9.3 Comparison of the Approaches

A comparison of the laser-induced temperature change ΔT_F to their respective estimated effective film thicknesses d_{eff} reveals the previously assumed and predicted inverse relationship between temperature and film thickness. The LAuNCs possess the smallest estimated effective film thickness and consequently exhibit the largest temperature rise, consistent across the pump-fluence-based and quasi-static strain based calculations. This trend explains the 47 % higher temperature found for the LAuNCs as their volume was determined to be 55 % of the AuNCs' volume. The slight discrepancy between 47 % and 55 % can be attributed to the approximate determination of the volume. In contrast, comparing the nanostructured sample's ΔT_η-values to the thin film's ones, a discrepancy can be found. While the quasi-static temperature increase of the AuNCs is 16.8 times larger than that of the thin film, their effective film thicknesses differ only by a factor of 1.46. Furthermore, additional discrepancies arise when comparing the thin film's results. The laser-induced temperature change of 15.9 K is nearly four times larger than the strain-based value of 4.2 K, which may be the result of an overestimated absorption coefficient.

Following the comparison of the results determined from different approaches, possible reasons for the discrepancies and the significantly larger temperature rise observed for the nanostructured samples are explored. A likely origin of the large differences between the measured ΔT_η and estimated ΔT_F for the AuNCs and LAuNCs is an underestimation of the absorbance. For the strain-based temperatures to match the fluence-based estimates, the absorbance would need to be approximately 20 % instead of the 3.72 % derived from the Fresnel equations for homogeneous films.

One detail to account for is the fact that, for nanostructures, absorption is not limited to the surface, as is the case for thin films. Instead, the geometric cross section of the cubes illuminated by the incident light has to be considered. A geometric correction for the cube's cross section yields an additional factor of $\sqrt{3}$, determined from the ratio of the cube's top face area to its illuminated lateral face area. This factor represents the upper limit for the possible additional absorption, corresponding to the orientation of the cubes with a maximal cross section. For other orientations relative to the incident light, the effective cross section decreases accordingly.

Additionally, the previous calculations were performed under the assumption that the nanostructures and thin film absorb the same fraction of light, which was assumed to be the perpendicular projected fluence $F_\perp = 10.7\ \text{mJ/cm}^2$. In reality, the nanostructures absorb a fraction of the total pump fluence of $F_{\text{full}} = 17\ \text{mJ/cm}^2$. Therefore, the expected temperature increase with respect to the corrections is:

$$\Delta T_{F,\text{corr}}^{\text{AuNC}} = \sqrt{3} \cdot Abs \cdot \frac{F_{\text{full}}}{C_V \cdot d \cdot \zeta_{\text{AuNC}}} = 30\ \text{K}, \tag{66}$$

$$\Delta T_{F,\text{corr}}^{\text{LAuNC}} = \sqrt{3} \cdot Abs \cdot \frac{F_{\text{full}}}{C_V \cdot d \cdot \zeta_{\text{LAuNC}}} = 74.2\ \text{K}. \tag{67}$$

However, the results still do not fully explain the large ΔT_η, as the estimated temperature rise of the nanoparticles is still a factor 2 too small.

Having taken the film thickness corrections into consideration, the transients of the three samples are depicted again, now normalized over their effective film thicknesses, as seen in fig. 25.

Recalling the initial expectation of an exclusively fluence- and volume-dependent scaling of the strain, coinciding normalized strain transients would be expected. However, fig. 25 reveals non-linearity, since the normalized transients do not overlap. The AuNCs' quasi-static strain amplitude is approximately 12 times larger than the thin film's, instead of the previous factor of 15 and the LAuNCs' amplitude is 10 times larger than the thin film's, instead of the previous 31 times. Interestingly, the difference between the nanoparticles is now only by a factor of 1.2 instead of the previous 2.1. It is important to note that the

normalization does not represent a temperature comparison, and instead, the amplitudes are proportional to the total absorbed fluence.

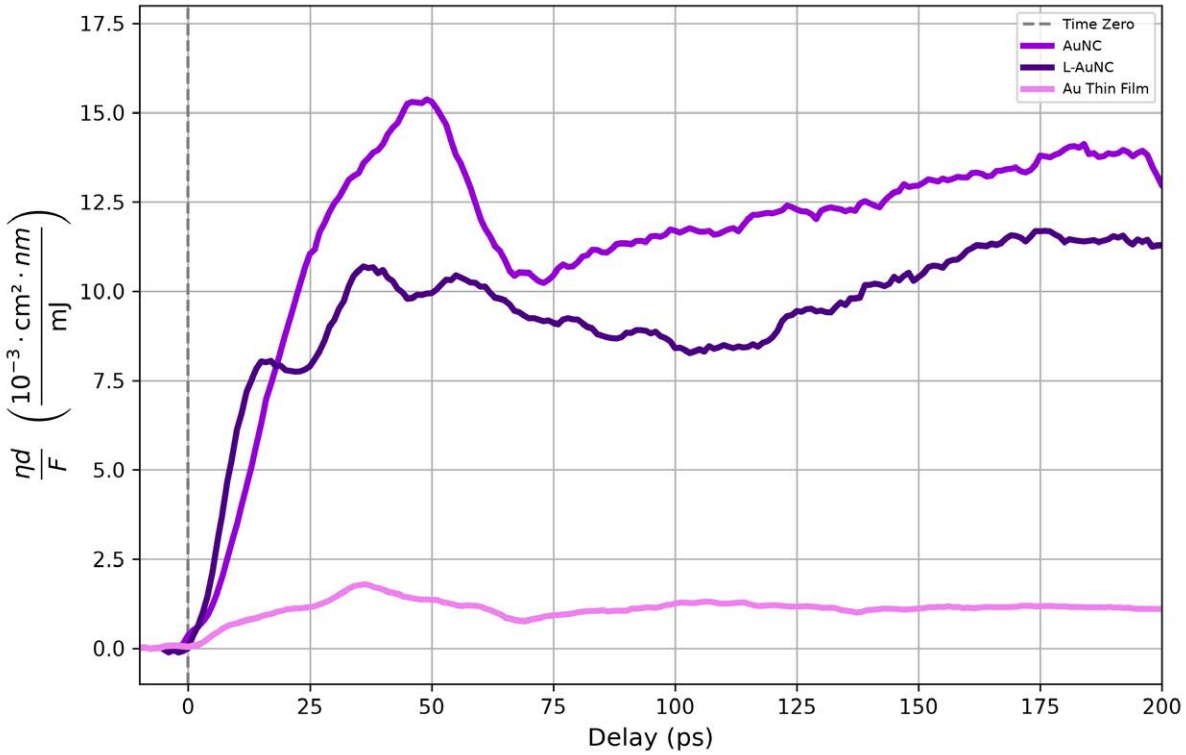

Figure 25: Comparison of the thin film's and nanoparticle's transient, normalized over their respective fluence and effective film thickness.

This remaining discrepancy leads to the conclusion that the absorption mechanics of the nanostructured samples are more complex than Fresnel absorption and likely originate from plasmon-enhanced absorption. Before discussing the latter, the calculated temperature changes are summarized again in table 5 below.

Sample	ΔT_η	ΔT_F	$\Delta\ \mathrm{T}_{F,\mathrm{corr}}$	d_{eff}	Utilized heat expansion coefficient
Gold thin film	4.2 K	15.9 K	15.9	100 nm	α_{uf}
AuNC	70.4 K	11.1 K	30 K	145.8 nm	α
LAuNC	147.9 K	26.98 K	74.2 K	58.94 nm	α

Table 5: Comparison of temperature changes determined from the measured quasi-static strain (ΔT_η), the strain calculated according to the fluence without plasmonic effects (ΔT_F), and according to the fluence absorbed in the corresponding volume ($\mathrm{T}_{F,\mathrm{corr}}$).

In metals such as gold, the quasi-free electrons are described as a free electron cloud, which can be displaced from its equilibrium position by an external electric field [60]. A restoring Coulombic force acts on the displaced electrons and results in their collective oscillation. The quantized oscillation is described by the quasi-particle plasmon, which can be driven resonantly by the incident light and enhances the local electromagnetic field and absorption.

In plasmonic nanoparticles, the intense evanescent[3] near-field can extend well beyond the physical bound-

[3]Evanescent describes the exponentially decaying electric field of the surface plasmons

aries of the particles, further increasing their absorption cross section [60,61]. Moreover, if two nanoparticles are brought into close proximity, their evanescent near-fields overlap and the resulting field in the junction center is greatly enhanced, creating hot spots for absorption.

While the differences between the nanoparticles and thin film can be explained by a fundamental difference in the absorption mechanics, as the nanoparticles are subject to plasmon-enhanced absorption in contrast to the thin film, the differences between the AuNCs and LAuNCs most likely originate from different plasmon-specific absorption mechanics. The normalization over the effective film thickness reveals that the LAuNCs' absorption efficiency is reduced compared to that of the AuNCs, which can be attributed to the complex nanostructuring of the LAuNCs shifting the localized surface-plasmon resonance away from the 800 nm pump wavelength. *S. Choi et al.* predict chiral hot spots along the concave gap surfaces of the LAuNCs, further backing up this hypothesis [4].

It is widely accepted that the localized surface plasmon resonance of such nanostructures is highly dependent on nanoparticle size, shape, and structure [62,63] and even subtleties in the nanostructure geometry can strongly affect the LSPR [4,64].

Another explanation for the different absorption efficiencies is the larger average interparticle distance between the individual LAuNCs of approximately 50 nm compared to the approximately 20 nm average distance between the individual AuNCs, which reduces the local field enhancement, as the enhancement is inversely dependent on this distance.

In their study, *A. Mizuno and A. Ono* investigated the LSPR frequency dependence on interparticle spacing for gold nanospheres. They find a red-shift of the LSPR for narrower interparticle spacing, due to stronger coupling between the nanoparticles [65]. They further highlight the fact that for periodic clusters or arrays of nanoparticles the collective plasmonic response becomes important. To summarize, plasmonic absorption is a likely candidate to explain the not overlapping normalized transients (fig. 25).

Even though the LAuNCs' absorption efficiency is reduced compared to AuNCs, they display the largest quasi-static temperature rise of $\Delta T(\eta_{\mathrm{qs}}) = 147.9$ K because of their much smaller volume and effective film thickness, over which the absorbed energy is distributed.

While the previous analysis and investigation of the nanostructured samples' large temperature change, suggesting plasmon-enhanced absorption, has been purely qualitative, a quantitative investigation is imperative and would include simulations based on the Mie theory, with which solutions for the LSPR can be found.

10 Overview

In this thesis, two types of gold nanoparticles, cubic and l-chiral-cubic nanoparticles, were investigated in the terms of their crystal structure and ultrafast strain dynamics in response to femtosecond laser-excitation. Additionally, a 100 nm gold thin film was investigated with the same methods as a reference for comparison.

For general characterization of the crystal lattice structure, static X-ray experiments were conducted. The generated reciprocal space maps revealed a bright twofold Au (111) Bragg reflection for the thin film, indicating the presence of two regions of differing morphology within the layer. In contrast, both nanostructured samples exhibited Au (111) and Au (002) Bragg reflections, broadened along the in-plane q_x- and q_y-dimensions, forming partial Debye-Scherrer rings. For both, the Au (002) reflections appear brighter than the Au (111) reflections, with the cubic nanoparticles even exhibiting a local maximum in the center of the partial ring. These findings indicate high crystallinity of the thin film and poly-crystallinity for the nanostructured samples, likely arising from the random orientation of the individual cubes. It is probable that the nanostructured samples are predominantly Au (002) oriented and the less bright Au (111) reflections originate either from a small portion of the cubes being tilted relative to the substrate and, therefore, appear as the Au (111) contribution or from unit cells that are tilted relative to the sample surface. A structure factor analysis of the observed crystal orientations lead to the conclusion that the differences in their peak intensity originate from differing lattice sums, i.e., the coherence length of the respective domains.

Ultrafast X-ray diffraction experiments were performed subsequently to assess the transient Bragg-peak shift associated with the transient lattice-spacing change along the out-of-plane q_z-dimension and presented the main focus of this thesis. For evaluating the peak shift, reciprocal space slicing (RSS) was utilized. For the evaluation of the thin film, the Au (111) reflection was considered and for the nanostructures, the Au (002) reflections were considered.

The thin film, excited with 17.8 mJ/cm^2, exhibits the same strain dynamics for both observed peak contributions, namely a nearly instantaneous expansion and subsequent damped oscillation around the quasi-static strain level of $0.2 \cdot 10^{-3}$, which is in line with previous studies of thin-film dynamics. Differences in amplitude between the peak contributions were observed and are linked to differing RSS factors. A Fourier Transform reveals odd harmonics, characteristic for a triangular strain pulse shape.

Next to characterizing the cubic nanoparticles' overall laser-induced strain response, the fluence-dependence of the strain evolution was investigated. All transients, irrespective of the excitation fluence, exhibit a similar appearance and scale almost linearly with increasing fluence. Like for the thin film, a nearly instantaneous out-of-plane expansion was observed, yet at a considerably larger amplitude. Instead of a damped oscillation, only two maxima, at 45 ps and 177 ps, were observed in the first 200 ps with oscillation periods of (33.5 $\pm$ 2.8) ps and (67.0 $\pm$ 11.2) ps, respectively. The first maximum exceeded that of the second one, amplitude-wise. The presence of a second harmonic indicates a more complex strain pulse shape. For longer timescales, after the different degrees of freedom, i.e., the electronic and phononic system, have equilibrated, an approximately 35 % relaxation of the strain level from the second maximum's level was observed. Further investigation by normalization of the transients, however, revealed slight non-linear scaling of the transient measured at the highest excitation fluence of 14.8 mJ/cm^2.

The chiral cubic nanoparticles were investigated in the same manner. Similarly, the transients measured for different excitation fluences scaled near-linearly. The overall appearance of the transients somewhat resembles the cubic nanoparticle ones, as they also exhibit two larger maxima, one immediately following excitation and the second one at approximately 200 ps. However, the second maximum reached approximately the same amplitude as the first oscillation. Additionally, the transients are modulated by smaller oscillations, likely stemming from the chiral overgrowth. The large oscillations possess a frequency of (9.9 $\pm$ 2.5) GHz and a period of (100.5 $\pm$ 25.3) ps. The smaller ones possess a frequency of (44.8 $\pm$

2.5) GHz and period of (22.4 ± 1.3) ps, which is not a harmonic, indicating a more complex strain pulse shape.

Fluence-normalization of the transients reveal a near-linear strain-fluence relationship again. However, slight non-linear scaling was found for the transient measured at the lowest excitation fluence of 5.8 mJ/cm^2. These non-linearities could be a result of imperfect overlapping of the pump and probe pulse on the samples and, therefore, incorrect determination of the pump fluence. It also suggests that the general strain response of the AuNCs and LAuNCs is much more complex than that of the thin films. Especially, given that the nanoparticle's morphologies are much more complex.

Calculations of the measured temperature change via the quasi-static strain amplitude reveal that the thin film heats up 4.2 K, the cubic nanoparticles 70.4 K and the l-chiral nanoparticles 147.9 K. This difference originates from plasmon-enhanced light absorption of the nanoparticles. Estimations of the expected laser-induced temperature change with consideration of the different sample volumes and absorption cross sections support this conclusion.

With this static and time-resolved characterization of the cubic and l-chiral cubic gold nanoparticles, the foundation for deeper investigation has been established.

Limitations and Outlook

While the qualitative framework for further investigation of the nanoparticles' strain dynamics and absorption mechanisms has been established, a detailed quantitative investigation must follow.

Specifically, the ultrafast strain evolution must be modeled. Difficulties arise because a simple 1D linear chain model is not sufficient to model the data, as it is for the thin film and instead, a 3D approach must be chosen [53]. Therefore, the udkm1dsim toolbox, utilized to model strain dynamics, must be extended to include this 3D case.

Lastly, the exact plasmon absorption mechanisms responsible for the different absorption efficiencies found for the nanoparticles need to be identified, e.g., by comparing the LSPR change for varying interparticle distances for both samples. Identifying the dominant factors influencing the LSPR, specifically for the l-chiral nanocubes, could further clarify the findings. Furthermore, a next step in research would be to record extinction spectra with both linearly polarized and circularly polarized light (circular dichroism studies) to identify the exact chiroptical properties. Ultrafast X-ray diffraction experiments utilizing circularly polarized pump pulses, circularly polarized Raman scattering experiments and calculations of the phonon dispersion could confirm whether or not chiral phonons are excited in the chiral nanoparticles.

References

[1] S. Liu, Z. Wu, Z. Zhu, K. Feng, Y. Zhou, X. Hu, X. Huang, B. Zhang, X. Dong, Y. Ma, K. Nie, J. Shen, Z. Wang, J. He, J. Wang, Y. Ji, B. Yan, Q. Zhang, A. Genest, X. Zhang, C. Li, B. Wu, X. An, G. Rupprechter, and L. He, "Quantifying the distinct role of plasmon enhancement mechanisms in prototypical antenna-reactor photocatalysts," Nat. Commun., vol. 16, no. 2245, 2025.

[2] M. Hentschel, M. Schäferling, X. Duan, H. Giessen, and N. Liu, "Chiral plasmonics," Sci. Adv., vol. 3, p. e1602735, 2017.

[3] K. Ishito, H. Mao, Y. Kousaka, Y. Togawa, S. Iwasaki, T. Zhang, S. Murakami, J.-i. Kishine, and T. Satoh, "Truly chiral phonons in -hgs," Nat. Phys., vol. 19, pp. 35–39, 2023.

[4] S. Choi, S. W. Im, J. H. Huh, S. Kim, J. Kim, Y.-C. Lim, R. M. Kim, J. H. Han, H. Kim, M. Sprung, S. Y. Lee, W. Cha, R. Harder, S. Lee, K. T. Nam, and H. Kim, "Strain and crystallographic identification of the helically concaved gap surfaces of chiral nanoparticles," Nat. Commun., vol. 14, no. 3615, 2023.

[5] H. Reddy, U. Guler, A. V. Kildishev, A. Boltasseva, and V. M. Shalaev, "Temperature-dependent optical properties of gold thin films," Opt. Mater. Express, vol. 6, pp. 2776–2802, 2016.

[6] D. I. Yakubovsky, A. V. Arsenin, Y. V. Stebunov, D. Y. Fedyanin, and V. S. Volkov, "Optical constants and structural properties of thin gold films," Opt. Express, vol. 25, pp. 25574–25587, 2017.

[7] A. Kossoy, V. Merk, D. Simakov, K. Leosson, S. Kéna-Cohen, and S. A. Maier, "Optical and structural properties of ultra-thin gold films," Adv. Opt. Mater., vol. 3, pp. 71–77, 2015.

[8] M. Nicoul, U. Shymanovich, A. Tarasevitch, D. von der Linde, and K. Sokolowski-Tinten, "Picosecond acoustic response of a laser-heated gold-film studied with time-resolved x-ray diffraction," Appl. Phys. Lett., vol. 98, p. 191902, 2011.

[9] J. Chen, W. K. Chen, J. Tang, and P. M. Rentzepis, "Time-resolved structural dynamics of thin metal films heated with femtosecond optical pulses," Proc. Natl. Acad. Sci., vol. 108, pp. 18887–18892, 2011.

[10] M. Mattern, A. von Reppert, S. P. Zeuschner, J.-E. Pudell, F. Kühne, D. Diesing, M. Herzog, and M. Bargheer, "Electronic energy transport in nanoscale au/fe hetero-structures in the perspective of ultrafast lattice dynamics," Appl. Phys. Lett., vol. 120, p. 092401, 2022.

[11] M. Mattern, A. von Reppert, S. P. Zeuschner, M. Herzog, J.-E. Pudell, and M. Bargheer, "Concepts and use cases for picosecond ultrasonics with x-rays," Photoacoustics, vol. 31, p. 100503, 2023.

[12] A. von Reppert, L. Willig, J.-E. Pudell, M. Rössle, W. Leitenberger, M. Herzog, F. Ganss, O. Hellwig, and M. Bargheer, "Ultrafast laser generated strain in granular and continuous fept thin films," Appl. Phys. Lett., vol. 113, p. 123101, 2018.

[13] A. H. Reid, X. Shen, P. Maldonado, T. Chase, E. Jal, P. W. Granitzka, K. Carva, R. K. Li, J. Li, L. Wu, T. Vecchione, T. Liu, Z. Chen, D. J. Higley, N. Hartmann, R. Coffee, J. Wu, G. L. Dakovski, W. F. Schlotter, H. Ohldag, Y. K. Takahashi, V. Mehta, O. Hellwig, A. Fry, Y. Zhu, J. Cao, E. E. Fullerton, J. Stöhr, P. M. Oppeneer, X. J. Wang, and H. A. Dürr, "Beyond a phenomenological description of magnetostriction," Nat. Commun., vol. 9, no. 388, 2018.

[14] J.-E. Pudell, M. Mattern, M. Hehn, G. Malinowski, M. Herzog, and M. Bargheer, "Heat transport without heating?—an ultrafast x-ray perspective into a metal heterostructure," Adv. Funct. Mater., vol. 30, p. 2004555, 2020.

[15] S. P. Zeuschner, J. E. Pudell, M. Mattern, M. Rössle, M. Herzog, A. Baldi, S. H. C. Askes, and M. Bargheer, "Unveiling the nanomorphology of hfn thin films by ultrafast reciprocal space mapping," Adv. Opt. Mater., vol. 12, p. 2400939, 2024.

[16] J. E. Pudell, M. Mattern, M. Herzog, A. von Reppert, C. K. Singh, D. Schick, M. Hehn, U. Boesenberg, A. Rodriguez-Fernandez, R. Shayduk, W. Jo, J. Möller, J. Hallmann, J. Wrigley, P. M. Oppeneer, A. Madsen, and M. Bargheer, "Electron pressure drives thz phonons in metal–metal superlattices," Nat. Commun., vol. 17, no. 5308, 2026.

[17] A. Bojahr, D. Schick, L. Maerten, M. Herzog, I. Vrejoiu, C. von Korff Schmising, C. Milne, S. L. Johnson, and M. Bargheer, "Comparing the oscillation phase in optical pump-probe spectra to ultrafast x-ray diffraction in the metal-dielectric $srruo_3/srtio_3$ superlattice," Phys. Rev. B, vol. 85, p. 224302, 2012.

[18] A. R. Shafiqa, A. Abdul Aziz, and B. Mehrdel, "Nanoparticle optical properties: Size dependence of a single gold spherical nanoparticle," J. Phys. Conf. Ser., vol. 1083, p. 012040, 2018.

[19] F. Stete, M. Bargheer, and W. Koopman, "Ultrafast dynamics in plasmon–exciton core–shell systems: the role of heat," Nanoscale, vol. 15, pp. 16307–16313, 2023.

[20] A. von Reppert, R. M. Sarhan, F. Stete, J. Pudell, N. Del Fatti, A. Crut, J. Koetz, F. Liebig, C. Prietzel, and M. Bargheer, "Watching the vibration and cooling of ultrathin gold nanotriangles by ultrafast x-ray diffraction," J. Phys. Chem. C, vol. 120, pp. 28894–28899, 2016.

[21] S. D. Namgung, R. M. Kim, and Y. C. Lim, "Circularly polarized light-sensitive, hot electron transistor with chiral plasmonic nanoparticles," Nat. Commun., vol. 13, no. 5081, 2022.

[22] Q. Cui, F. He, X. Wang, B. Xia, and L. Li, "Gold nanoflower@gelatin core–shell nanoparticles loaded with conjugated polymer applied for cellular imaging," ACS Appl. Mater. Interfaces, vol. 5, 2013.

[23] X. Huang, I. H. El-Sayed, W. Qian, and M. A. El-Sayed, "Cancer cells assemble and align gold nanorods conjugated to antibodies to produce highly enhanced, sharp, and polarized surface raman spectra: A potential cancer diagnostic marker," Nano Lett., vol. 7, pp. 1591–1597, 2007.

[24] G. Von Maltzahn, J. H. Park, A. Agrawal, N. K. Bandaru, S. K. Das, M. J. Sailor, and S. N. Bhatia, "Computationally guided photothermal tumor therapy using long-circulating gold nanorod antennas," Cancer Res., vol. 69, pp. 3892–3900, 2009.

[25] M. C. Daniel and D. Astruc, "Gold nanoparticles: Assembly, supramolecular chemistry, quantum-size-related properties, and applications toward biology, catalysis, and nanotechnology," Chem. Rev., vol. 104, pp. 293–346, 2004.

[26] H. Chen and C. Hao, "Recent advances in chiral gold nanomaterials: From synthesis to applications," Molecules, vol. 30, p. 829, 2025.

[27] C. Corti and R. Holliday, eds., Gold: Science and Applications. CRC Press Taylor & Francis Group, 2021.

[28] M. N. Polyanskiy, "Refractiveindex.info database of optical constants," Sci. Data, vol. 11, p. 94, 2024.

[29] G. P. Moss, "Basic terminology of stereochemistry (iupac recommendations 1996)," Pure Appl. Chem., vol. 68, pp. 2193–2222, 1996.

[30] Y. C. Lim, R. M. Kim, J. H. Han, I. Aharonovich, K. T. Nam, and S. Kim, "Strong chiral response of chiral plasmonic nanoparticles to photonic orbital angular momentum," Adv. Opt. Mater., vol. 13, p. 2402268, 2025.

[31] S. W. Im, R. M. Kim, J. H. Han, I. H. Ha, H.-E. Lee, H.-Y. Ahn, E. Jo, and K. T. Nam, "Synthesis of chiral gold helicoid nanoparticles using glutathione," Nat. Protoc., vol. 20, pp. 1082–1096, 2025.

[32] M. Swierczewski and T. Burgi, "Langmuir and langmuir–blodgett films of gold and silver nanoparticles," Langmuir, vol. 39, pp. 2135–2151, 2023.

[33] S. Deb and G. Chel, "Langmuir–blodgett films: A unique approach towards monomolecular assemblies," in Defects Engineering in Electroceramics for Energy Applications, Springer Singapore, 2024.

[34] D. Schick, R. Shayduk, A. Bojahr, M. Herzog, C. von Korff Schmising, P. Gaal, and M. Bargheer, "Ultrafast reciprocal-space mapping with a convergent beam," J. Appl. Crystallogr., vol. 46, pp. 1372–1377, 2013.

[35] J. Als-Nielsen and D. McMorrow, Elements of Modern X-Ray Physics, vol. 55. John Wiley & Sons, Ltd, 2002.

[36] C. Kittel, Introduction to Solid State Physics. John Wiley & Sons, Inc, 2005.

[37] R. Gross and A. Marx, Festkörperphysik. Oldenbourg Verlag München, 2012.

[38] S. P. Zeuschner, M. Mattern, J.-E. Pudell, A. von Reppert, M. Rössle, W. Leitenberger, J. Schwarzkopf, J.-E. Boschker, M. Herzog, and M. Bargheer, "Reciprocal space slicing: A time-efficient approach to femtosecond x-ray diffraction," Struct. Dyn., vol. 8, p. 014302, 2021.

[39] A. von Reppert, "Ultrafast magnetostriction in dysprosium studied by femtosecond x-ray diffraction," Master's thesis, Universität Potsdam, 2015.

[40] S. P. Zeuschner, Magnetoacoustics observed with Ultrafas X-ray Diffraction. PhD thesis, Universität Potsdam, 2015.

[41] J.-E. Pudell, "Ultraschnelle magnetostriktion von antiferromagnetischem holmium," Master's thesis, Universität Potsdam, 2015.

[42] U. Pietsch, V. Holý, and T. Baumbach, High-Resolution X-Ray Scattering. Springer New York, NY, 2004.

[43] D. Kriegner, E. Wintersberger, and J. Stangl, "Xrayutilities: A versatile tool for reciprocal space conversion of scattering data recorded with linear and area detectors," J. Appl. Crystallogr., vol. 46, pp. 1162–1170, 2013.

[44] E. Grüneisen, "Theorie des festen zustandes einatomiger elemente," Ann. Phys., vol. 344, pp. 257–306, 1912.

[45] D. Strickland and G. Mourou, "Compression of amplified chirped optical pulses," Opt. Commun., vol. 56, pp. 219–221, 1985.

[46] C. von Korff Schmising, M. Bargheer, M. Kiel, N. Zhavoronkov, M. Woerner, T. Elsaesser, I. Vrejoiu, D. Hesse, and M. Alexe, "Accurate time delay determination for femtosecond x-ray diffraction experiments," Appl. Phys. B, vol. 88, pp. 1–4, 2007.

[47] A. von Reppert, Magnetic strain contributions in laser-excited metals studied by time-resolved X-ray diffraction. PhD thesis, Universität Potsdam, 2021.

[48] M. Bargheer, N. Zhavoronkov, M. Woerner, and T. Elsaesser, "Recent progress in ultrafast x-ray diffraction," ChemPhysChem, pp. 783–792, 2006.

[49] W. Press, S. Teukolsky, W. Vetterling, and B. Flannery, "Numerical recipes," Cambridge, UK, Cambridge University Press, 1992.

[50] J. W. Cooley and J. W. Tukey, "An algorithm for the machine calculation of complex fourier series," Math. Comput., vol. 19, pp. 297–301, 1965.

[51] Y. A. Chang and L. Himmel, "Temperature dependence of the elastic constants of cu, ag, and au above room temperature," J. Appl. Phys., vol. 37, pp. 3567–3572, 1966.

[52] D. Schick, M. Herzog, A. Bojahr, W. Leitenberger, A. Hertwig, R. Shayduk, and M. Bargheer, "Ultrafast lattice response of photoexcited thin films studied by x-ray diffraction," Struct. Dyn., vol. 1, no. 064501, 2014.

[53] A. von Reppert, L. Willig, J.-E. Pudell, M. Rössle, W. Leitenberger, M. Herzog, F. Ganss, O. Hellwig, and M. Bargheer, "Ultrafast laser generated strain in granular and continuous fept thin films," Appl. Phys. Lett., vol. 113, p. 123101, 2018.

[54] J.-E. Pudell, M. Mattern, F. Baltrusch, F. L. Boariu, M. Kronseder, R. Shayduk, A. Madsen, M. Rössle, M. Bargheer, D. Schick, and A. von Reppert, "Ultrafast x-ray thermometry: Contrasting strain and debye-waller effects in platinum thin films," Phys. Rev. B, vol. 113, p. L220301, 2026.

[55] F. C. Nix and D. MacNair, "The thermal expansion of pure metals: Copper, gold, aluminum, nickel, and iron," Phys. Rev., vol. 60, pp. 597–605, 1941.

[56] P. B. Johnson and R. W. Christy, "Optical constants of the noble metals," Phys. Rev. B, vol. 6, pp. 4370–4379, 1972.

[57] M. Born and E. Wolf, Principles of optics: electromagnetic theory of propagation, interference and diffraction of light. Elsevier, 2013.

[58] T. H. Geballe and W. F. Giauque, "The heat capacity and entropy of gold from 15 to 300° k.," J. Am. Chem. Soc., vol. 74, pp. 2368–2369, 1952.

[59] Y. Takahashi and H. Akiyama, "Heat capacity of gold from 80 to 1000 k," Thermochim. Acta, vol. 109, pp. 105–109, 1986.

[60] S. A. Maier, Plasmonics: Fundamentals and Applications. Springer New York, NY, 2007.

[61] L. Novotny and B. Hecht, Principles of nano-optics. Cambridge university press, 2012.

[62] E. Ringe, J. M. McMahon, K. Sohn, C. Cobley, Y. Xia, J. Huang, G. C. Schatz, L. D. Marks, and R. P. Van Duyne, "Unraveling the effects of size, composition, and substrate on the localized surface plasmon resonance frequencies of gold and silver nanocubes: A systematic single-particle approach," J. Phys. Chem. C, vol. 114, pp. 12511–12516, 2010.

[63] P. V. Demydov, A. M. Lopatynskyi, I. I. Hudzenko, and V. I. Chegel, "The approaches for localized surface plasmon resonance wavelength position tuning. short review," Semicond. Phys. Quantum Electron. Optoelectron., vol. 24, pp. 304–311, 2021.

[64] C. L. Nehl and J. H. Hafner, "Shape-dependent plasmon resonances of gold nanoparticles," J. Mater. Chem., vol. 18, pp. 2415–2419, 2008.

[65] A. Mizuno and A. Ono, "Static and dynamic tuning of surface plasmon resonance by controlling interparticle distance in arrays of au nanoparticles," Appl. Surf. Sci., vol. 480, pp. 846–850, 2019.

Danksagung

Zuletzt möchte ich mich bei den Menschen bedanken, die diese Arbeit ermöglicht haben.

An erster Stelle danke ich Dr. Steffen Zeuschner, der mich während der gesamten Arbeit begleitet und unterstützt hat, sei es im Labor, bei der Auswertung der Messdaten oder beim Verfassen der Arbeit. Ich danke dir, lieber Steffen, für deine Geduld und deine überaus freundliche und engagierte Art der Unterstützung und Motivation während des Projektes. Ich habe viel von dir gelernt und hoffe, dass ich davon einiges in meine zukünftige Arbeit einbringen kann.

Ich danke Prof. Dr. Matias Bargheer sowie der gesamten UDKM-Gruppe für die Gelegenheit, diese Arbeit in einer so freundlichen und offenen Atmosphäre durchzuführen, sowie dafür, dass meine Arbeit stets mit Interesse verfolgt und mit Fachwissen unterstützt wurde.

Meiner Familie und meinen Freunden danke ich für die Liebe, Motivation und Unterstützung, die mich nicht nur durch diese Zeit, sondern durch das gesamte Studium getragen haben.

Selbstständigkeitserklärung

Hiermit versichere ich, dass ich, **Franziska Jäger**, die vorliegende Arbeit ohne Hilfe Dritter und ohne Zuhilfenahme anderer als der angegebenen Quellen und Hilfsmittel angefertigt habe. Die den benutzten Quellen wörtlich oder inhaltlich entnommenen Stellen sind als solche kenntlich gemacht.

Die „Richtlinie zur Sicherung guter wissenschaftlicher Praxis für Studierende an der Universität Potsdam (Plagiatsrichtlinie) - Vom 18. November 2020", im Internet unter https://www.uni-potsdam.de/fileadmin/projects/ambek/Amtliche_Bekanntmachungen/2020/ambek-2020-19-937-944.pdf, habe ich zur Kenntnis genommen.

Die Arbeit wurde bisher in gleicher oder ähnlicher Form keiner anderen Prüfungsbehörde vorgelegt und auch nicht veröffentlicht.

Zur grammatischen Korrektur und Formulierungshilfe wurde KI genutzt.

Potsdam, 18.08.2026 — Ort, Datum

F. Jäger — Unterschrift